The Effect of Anisotropy Dimensions on the Self-Assembly of Nanoparticles

by

Daniel Ortiz

A dissertation submitted in partial fulfillment
of the requirements for the degree of
Doctor of Philosophy
(Material Science and Engineering)
in The University of Michigan
2014

Doctoral Committee:

Professor Sharon C. Glotzer, Chair
Professor Nicolas A. Kotov
Professor Joanna M. Millunchick
Professor Michael J. Solomon

I dedicate this thesis to the two important woman in my life: my mother, for her firm support and guidance, and Alex for being everything to me.

ACKNOWLEDGEMENTS

I would like to thank my advisor Sharon Glotzer and my comittee for guidance throughout my thesis. I would like to thank my collaborators and Glotzer labmates for without their contribution this thesis would not be possible.

TABLE OF CONTENTS

LIST OF FIGURES

Figure

CHAPTER I

Introduction

Anisotropy dimensions *Glotzer and Solomon* (2007) are the chosen paradigm to understand the effect of different chemical transformations on self-assembly. Anisotropy dimensions are a set of geometric and energetic transformations that can be used to categorize and understand nanomaterials. *Glotzer and Solomon* (2007) The systematic investigation of anisotropy dimensions presupposes the ability of chemists to control and transform nanoparticle shape and surface chemistry. Nanoparticle shape control *Tao et al.* (2008) is used to synthesize bulk quantities of specific geometries, such as nanoellipses *Liu et al.* (2012a), nanopolyhedra *Damasceno et al.* (2012a), and patchy particles *Glotzer* (2004). The incredible shape control capable by chemists motivates the need to understand the effect of shape on self-assembly systematically so as to engineer, categorize, and understand nanoparticles. Nanomatrial shape transformations transform a building block's geometry, such as from a cube to a tetrahedron.*Fan et al.* (2008) These shape transformations can occur via external stimuli, such as photodecomposition *Jin et al.* (2001). The surface chemistry and shape of the nanomaterial effect the bulk properties of the material by controlling the types of crystal structures observed as a result of self-assembly. Self-assembly is when a disordered system of nano components forms an ordered pattern via the minimization of free energy without an external driving force. *Whitesides and Grzybowski*

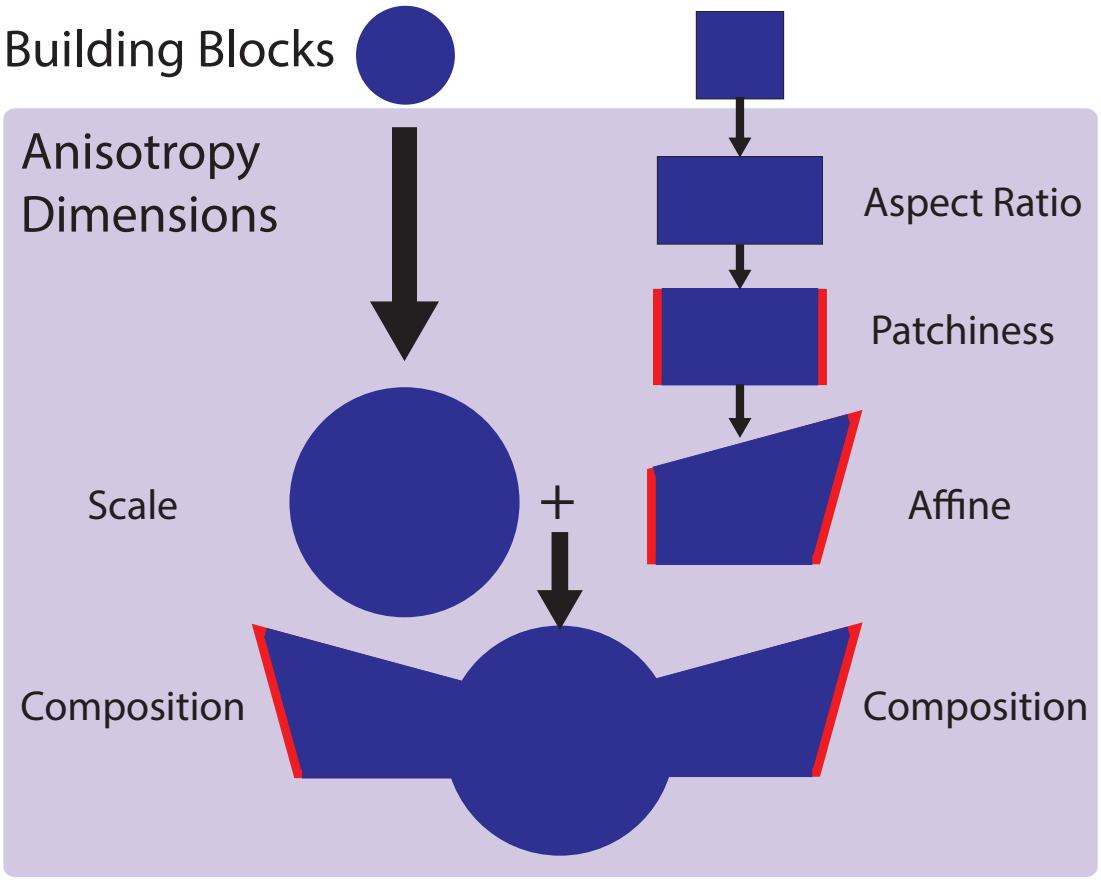

Figure 1.1: A representative example of how to use anisotropy dimensions to construct an exotic nanoparticle is summarized above. A square and triangle are transformed using the scale, aspect ratio, patchiness, and affine anisotropy dimensions. The two transformed building blocks are transformed through composition into an exotic nanoparticle.

(2002) Computer simulations were used to model the effect of each anisotropy dimensions on self-assembly. Self-assembly experiements were performed using molecular dynamics and monte carlo simulations to uncover the equilbrium configurations of these nanomaterials. *Metropolis and Ulam* (1949); *Alder and Wainwright* (1959)

Although anisotropy dimensions provide a conceptual framework to categorize different nanoparticles, the anisotropy dimensions of a nanoparticle are not a predictive tool. Anisotropy dimensions do not provide insight into their effect on self-assembly. It is clear that arbitrary nanoparticles can be designed from simple precursors with a collection of transformation. (See Figure 1.1) This design of an exotic nanoparticles

can be decomposed into a collection of transformations upon different anisotropy dimensions. (See Figure 1.1) A nanodisk and nanosquare through the scaling, aspect ratio, patchiness, affine, and composition transformation can be used to form an exotic nanoparticle. (See Figure 1.1) Each anisotropy dimension used to synthesize this exotic nanoparticle has a chemical shape control counterpart. The scaling transformation, or size control, can be controlled by altering ligand concentration. *Teranishi and Miyake* (1998) The aspect ratio transformation in inorganic nanoparticles can be controlled by the ratio of metal salts to seeds. *Jana et al.* (2001) Patchiness can be functionalized on anisotropic nanomaterials by the controlled growth of nanoparticle edges with different crystallographic facets. *Ye et al.* (2013c) General affine transformations can be controlled via overgrowth processes. *Tsuji et al.* (2010) The composition trasformation can be controlled by oriented attachment. *Liu et al.* (2012b) The grand challenge is to systematically understand the effect of each transformtion on self-assembly so that reverse engineering of nanoparticles becomes an exact science.

1.1 Shape Control of Nanomaterials

The facile synthesis of anisotropic nanomaterials by wet synthetic procedures is one of the major revolutions in nanomaterials. The ability to synthesize large quantities of nanomaterials is necessary to scale up these exciting materials for industry. Anisotropic nanomaterials have a long hisotry. Single crystals of semiconductor wires were demonstrated in the 1960s via Vapor Liquid Solid mechanism *Wagner and Ellis* (1964). However, a facile scalable synthesis procedure for metallic nanorods was only demonstrated recently. *Murphy et al.* (2006) The formation of these faceted nanomaterials proceeds in two steps. The first step in the reaction pathway from metal precursors to metallic nanomaterials is a burst of nucleation that forms seeds with distinct internal crystallographic structures. *Xia et al.* (2009b) Generally, the internal crystallographic structure will be single crystal, singly twinned, multiply twinned, or

a plate with stacking faults. *Iijima and Ichihashi* (1986); *Ajayan and Marks* (1988); *Nikoobakht and El-Sayed* (2003); *Hofmeister et al.* (2002) The second step involves the directed growth of crystallographic facets. By altering the growth rate via surface ligands of different crystallographic facets, faceted nanoparticles ranging from cuboctahedron to triangular nanoplates can be synthesized.

Selective capping agents, and seeded growth alter the shape evolution from nanocrystalline seed to the nanoparticle. The chemisorption of capping agents onto specific crystallographic facets slows the growth rate of specific facets and alters the shape of the end product. The adsorption of H_2 gas on a spherical nanocrystal can cause the transformation of Pt spherical nanocrystal into a a nanocube.*Harris* (1986) The surface capping agent can arise from the decomposition of metal salts such as in adsorped CO. *Joshi et al.* (2006) The addition of PVP to the decompsition reaction of Ag salts preferentially binds to the $< 100 >$ facets stabilizing Ag nanocubes.*Sun and Xia* (2002) Multiple capping agents can be added to cooperatively form different nanocrystalline shapes. By mixing ratio the CTAB capping agent with bromide seeds, the shape of the gold can be altered from rectangular, square, to tetrapodal.*Sau and Murphy* (2007) Seeded growth of Ag on nanocubes can transform nanocubes into nanoctahedra via overgrowth. *Tao et al.* (2006) Heteroepitaxial growth of Pd on cubic Pt can transform the effective core-shell nanoparticle shape from a nanocube to an octahedron.*Habas et al.* (2007) The use of capping agents and seeds provides the synthetic tools needs to control the shape of nanoparticles.

1.2 Shape Transformations in Nanomaterials

Radiation is a powerful tool to deform the effective shape of a nanoparticle. Silica colloids with a 14 MeV Au ion beam transformed the spherical colloids into ellipsoids.*Van Dillen et al.* (2001) Photoreduction of silver can transform silver nanodisks to nanotriangles reversibly. *Lee et al.* (2009) There are strong indications that light-

driven shape transformations in Ag nanoparticles follow an Arrhenius light-mediated 2D coalesence process.*Lee et al.* (2013) The length of silver nanorods can be controlled by the wavelength of light where the surface plasmon resonance of Ag spherical seeds causes anisotropic growth.*Zhang et al.* (2011a) At larger length scales, sheets of assembled CdTe nanoparticles will transform into helical ribbons with controllable pitch. *Srivastava et al.* (2010) Electron irradiation fransform CdS nanorods with Au tips into spherical core-shell Cd/AuS with an intermediate Cd/AuS rectangular prism.*van Huis et al.* (2011) The use of radiation can lead to shape transformations that elongated, truncate, distort, or twist anisostropic nanoparticles.

Active materials are means of obtaining shape transformations. Uniform polymer deformations can be engineered to form switchable high density nanogap structures with tunable optical properties.*Ross et al.* (2011) Polymeric vesicles made from block copolymers can undergo a shape transformation from tubules to spheres in the presence of cross-linkers.*van Oers et al.* (2013) Magnetic stirring of polystyrene in an organic solvent leads to the shape transformation between a sphere and a disk.*Liu and Wang* (2012) Polymeric nanoparticles can be used in targeted drug delivery for cancer by undergoing a hydrophobic to hydrophillic transition that swells the polymeric cage and releases the drug contents.*Griset et al.* (2009) Ellipsoidal P4VP/PS can be reversibly transformed to spherical P4VP/PS via swelling caused by solvent annealing.*Deng et al.* (2013) Surface tension driven assembly of folded polyhedra made from metallic plates open opportunities to synthesize highly assymetric polyhedra that would be difficult to synthesisze from wet chemical means.*Leong et al.* (2007b) Polymerization of silicon oil emulstions of 3-methacryloxypropyl trimethoxysilane(TPM) produces buckled colloids that can provide lock-key binding mechanism. *Sacanna et al.* (2010) The use of materials that can alter their shape or configuration dynamically open up the possibility of dynamic multifunctional matter.

1.3 Self-Assembly of Nanomaterials

Patchy colloids *Glotzer* (2004); *Zhang et al.* (2005b) are colloids with discrete attractive interaction sites that allow colloids to be rationally designed from the bottom up. The self-assembly of patchy colloids provides a means of crystallizing interesting crystal structures. Beyond the structural diversity of patchy particles, patchy particles form reversible gels *Sciortino and Zaccarelli* (2011), and crystal structures with tunable optical properties*McConnell et al.* (2010). Recent advances in chemistry *Du and O'Reilly* (2011); *Chen et al.* (2011) show that a self-assembly paradigm has formed by the careful design of the size, location, and distribution of patches. The Archimedean tiling have been sythesized by placing patches on spherical particles.*Antlanger et al.* (2011) Janus colloids have been shown to assemble the Kagome lattice.*Chen et al.* (2011) By altering the opening angle of the patches, the self-assembly changes from chains to porous squares.*Chen et al.* (2012a) Reversible hydrophobic patches made with host-guest supramolecular chemistry assembles reversible networks whose fractal dimension can be tuned.*Hermans et al.* (2009) Patchy colloids provide a conceptual and experimental framework for the self-assembly of nanomaterials.

The self-assembly of faceted nanoparticles provides a means of forming crystal structures that would be hard to achieve with patchy colloids. Uniform polyedral silver nanopolyhedra self-assemblies form the densest known packing crystal structure of cubes truncated cubes and octahedra.*Henzie et al.* (2011) 2D self-assembly of colloidal concave octapods show the that by tuning the pod/diameter length ratio that rhombic crystal structures and hexagonal rotator phases form.*Qi et al.* (2012) Simulations of a family of hard polyhedra show the assembly of rotator crystals, plastic crystals, and quasicrystals.*Damasceno et al.* (2012a) Binary mixtures of convex and concave nanoplates highlights how shape complementary can guide self-assembly.*Paik and Murray* (2013) Without shape complementarity, binary mixtures of convex polyhedra were found to phase seperate except when the order disorder transition pressure

was close. *Khadilkar et al.* (2013) The competition between shape and ligand mediated enthalpic patches can lead to interesting phase behavior. The phase behavior of nanocubes, which can be tuned by ligand concentration, contains rhombohedral and simple cubic crystal structure. *Zhang et al.* (2011c) The competition between shape and enthalpic interactions in nanoplates has been shown to stabilize nontrivial alternating patterns. *Ye et al.* (2013b)

1.4 Properties of Nanomaterials

The optical catalytic magnetic and electrical properties of nanomaterials can depend greatly on the shape of the building blocks. The anisotropic plastic deformation of silica colloids via irradiation has been shown to tune the optical properties of assemblies. *Velikov et al.* (2002) The shape of a Pt nanoparticle can affect its catalytic properties by altering the onset temperature of 2-propapnol oxidation reaction. *Mostafa et al.* (2010) Catalytic cycling decreases the sharpness of facets in colloidal transition metal nanocatalysts and decreases catalytic performance.*Narayanan and El-Sayed* (2005) A comparision between spherical and cubic magnetic $\gamma - Fe_2O_3$ assemblies shows that the blocking temperature is lower for cubic assemblies. *Salazar-Alvarez et al.* (2008) The shape of CdSe affects the charge seperation and transport dynamics of bulk heterojunction nanoparticle solar cells.*Dayal et al.* (2010) The selection of shape is key to carefully tuning the material properties of nanoparticle assemblies.

The adsorption, electrical, antibacterial, and mechanical properties of nanomaterials can depend greatly on the surfactants used for nanoparticle stability. For intravenous biomedical applications, nanoparticle coatings need to be modified to inhibit removal from the bloodstream by phagocytosis. *Gref et al.* (2000) The interactions between surface ligands and the lipid bilayer of cells is critical to applications such as drug/gene delivery. *Verma and Stellacci* (2010) The metal insulator transition in nanoparticles is controlled by the length of the polymer surfactant chain. In silver

quantum dots monolayers, the metal insulator transition occurs around 5 $\mathring{A}$ seperation distance.*Collier et al.* (1997) The magnetic coercivity of $MnFe_2O_4$ nanoparticles is strongly altered by the coordination of the surface ligands. *Vestal and Zhang* (2003) Ligands can hinder the antibacterial properties of silver nanoparticles by limiting bioavailability and toxicity of silver ions.*Xiu et al.* (2011) The length of the ligands significantly effects the elastic moduli and hardness of assembled nanocrystalline structures.*Tam et al.* (2010) Surface ligands can effect absorption, electronic, antibacterial and mechanical properties of nanomaterials.

1.5 Contributions

The main body of the thesis is divided into three parts. The first part is on the self-assembly of colloidal molecules, which highlights how reconfigurability anisotropic colloidal molecules can self-assemble crystalline structures with no experimental analogue. The second part is on the work self-assembly of Archimedean tilings, which quanitifies and explains the degree of interaction selectivity needed to self-assemble each Archimedean tiling. The last part is on the effect of shape transformations on self-assembly and explores the effect of shape on the self-assembly of irregular nanoplates.

CHAPTER II

Self-assembly and reconfigurability of colloidal molecules

2.1 Abstract

The lock-and-key colloidal particles of Sacanna et. al. *Sacanna et al.* (2010) are novel dynamic building blocks consisting of a central spherical colloidal particle (key) attached to a finite number of dimpled colloidal particles (locks) via depletion interactions strong enough to bind the particles together but weak enough that the locks are free to rotate around the key. This rotation imbues a mechanical reconfigurability to these colloidal molecules. Here we use molecular simulation to predict that these lock-and-key building blocks can self-assemble into a wide array of complex crystalline structures that are tunable via a set of reconfigurability dimensions: the number of locks per building block, bond length, size ratio, confinement, and lock mobility. We demonstrate that, with reconfigurability, ordered structures such as random triangle square tilings assemble, despite being kinetically inaccessible with non-reconfigurable but similar building blocks.

2.2 Introduction

The use of anisotropic colloidal particles in the self-assembly of crystalline materials with non-trivial structure has grown tremendously with the development of new synthesis techniques that offer unprecedented control over colloidal geometry and interactions. *Sacanna et al.* (2010) These advances have opened many new directions for the self-assembly of functional materials made from colloidal molecules, bio-inspired aggregates and hierarchical assemblies. *Li et al.* (2009a); *Mitragotri and Lahann* (2009); *Miszta et al.* (2011) Colloidal molecules with valence and specific directional binding allow the synthesis of low coordination building blocks that are common in small molecular systems. *Wang et al.* (2012) Using lock and key colloidal synthesis, colloidal atoms can be built from the bottom up, allowing for the development of materials with tunable and multifunctional properties. *Sacanna et al.* (2010) Self-assembly of colloidal polymers into lock and key colloids has been shown to depend sensitively on the colloidal indentation size of the locks. *Ashton et al.* (2013) Colloidal molecules have been used to create antireflective materials *Koo et al.* (2004), plasmon sensors *Cheng et al.* (2011), or as the building blocks for a 3D photonic crystal. *Liddell and Summers* (2003)

The rational design of functional materials allows individually designed attributes to be programmed prior to assembly. *Glotzer and Solomon* (2007); *van Blaaderen* (2006) Although self-assembly has proven to be a worthy candidate to organize these complex building blocks, competitive structures can become kinetically trapped, inhibiting desirable, stable crystalline structures. *Solomon et al.* (2010)

Shape change at the building block level can facilitate the self-assembly of kinetically hindered configurations. *Nguyen et al.* (2011) In a similar manner to driven systems, where emergent behavior is readily seen *McCandlish et al.* (2012); *Nguyen et al.* (2012); *Marchetti* (2012), reconfigurable colloidal building blocks with an intrinsic dynamism may also exhibit emergent phases that are not available to the static

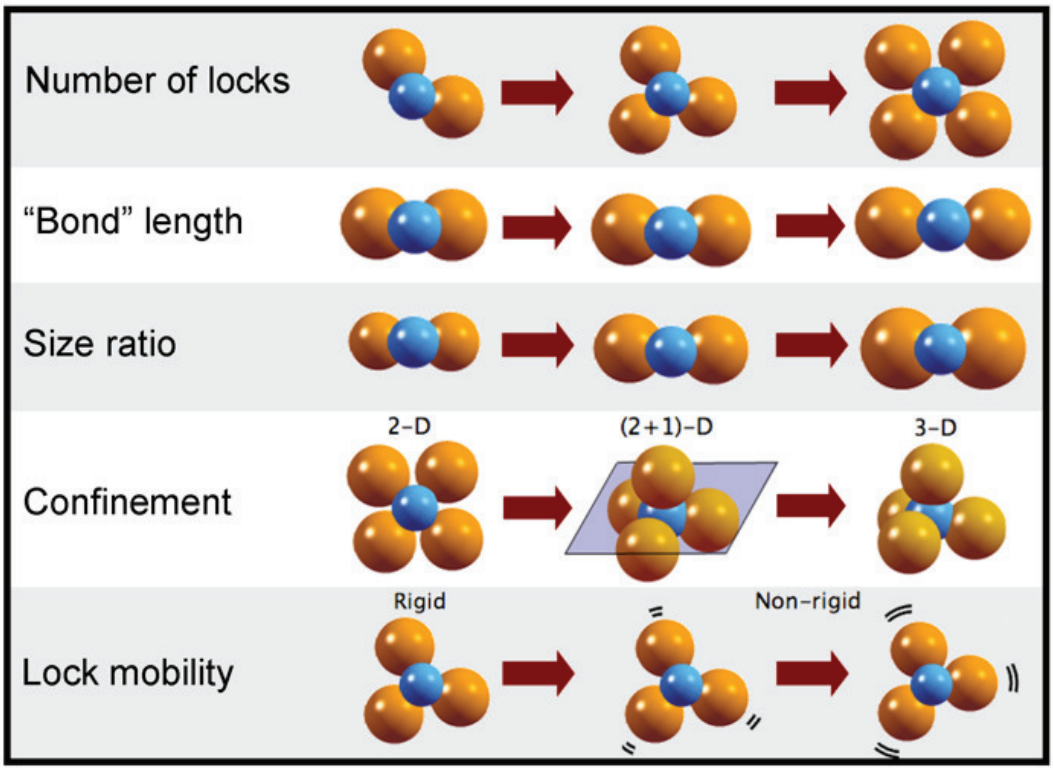

Figure 2.1: Reconfigurability dimensions of colloidal molecules are described above. The building blocks have a rich design space that can be accessed and toggled during the assembly process. The first three parameters: lock number, bond length, and the size ratio directly control the geometry of the cluster, while the particle confinement and lock mobility control the configurations the cluster can access.

building block. Shape change in lock and key colloids can occur via external stimuli *Motornov et al.* (2007) or by changing the sample. The changes in shape or interaction can further lead to significantly different macroscopic properties such as mechanical and rheological properties. *Kohlstedt and Glotzer* (2013) Building block shape reconfiguration plays a key part in achieving programmable building blocks with the ability to assemble complex hierarchical structures. *Klavins* (2007); *Nguyen et al.* (2011) Beyond the progress that has been made using mixtures of charged spherical colloids, hard shapes and patchy particles to stabilize atomic crystals *Dong et al.* (2010); *Leunissen et al.* (2005) and quasicrystalline structures *Talapin et al.* (2009),

reconfigurability in colloidal molecules adds a new design dimension for colloids.

In this study, we predict that lock-and-key colloidal particles like those described in *Sacanna et al.* (2010), are able to self-assemble into non-trivial ordered structures depending on the building block geometry and boundary conditions. These building blocks are intrinsically reconfigurable because the locks can rotate freely around the keys. The paper is organized as follows. In section 2.3, we introduce the model and simulation methods. In section 2.4, we organize our results into subsections of increasing complexity. The assembled structures are organized into geometric phase diagrams of reconfigurable colloidal molecules. In section 2.5, we provide a discussion and outlook. The results presented here serve as proofs of concept that reconfigurable colloids are promising candidates for engineering reconfigurable nanostructures from the bottom up, and thus, motivate further experimental exploration of this unique family of building blocks

2.3 Model

We classify the lock-and-key colloids by five reconfigurabilty dimensions: Number of locks (N_L), lock-key bond length (d_{LK}), lock-key size ratio (D_L/D_K), building block confinement (2D-, quasi3D-, and 3D-), and building block lock mobility (γ_r). These reconfigurability dimensions are summarized in Figure 2.1.

We use the following model to represent the lock-and-key building blocks (Fig. 2.1a). Each building block consists of N_L locks of diameter D_L connected by a central key of diameter D_K. We consider only building blocks with one key connected to N_L identical locks. We fix D_K=1 for all simulations and report the size ratio as simply D_L. Thus, D_K is the unit of length in our simulations. . The bond distance δ is related to d_{LK} by $2\delta = 1 + D_L - 2d_{LK}$, Because the depletion attraction strength between the dimpled locks and the key is on the order of $10k_BT$ *Sacanna et al.* (2010), it is reasonable to assume that the locks permanently attach to the key, and thus we

constrain the centre-to-centre distance between the lock and the key throughout our simulations.

In all simulations, we assume that the depletion mediated binding of locks to keys has already occurred, and focus our attention on the assembly of the resulting building blocks. The interaction between the locks and keys is modeled by an excluded volume interaction due to the double-layer repulsion between the charged colloids and a short-range attraction due to depletion interactions between intra- and inter-building block volume overlaps *Sacanna et al.* (2010). The excluded volume electrostatic repulsion (U_e) is modeled by the Yukawa potential, integrated over the surface of the spherical colloid in the Derjaguin limit *Derjaguin* (1934), and shifted to the colloid surface where Z is an energetic constant based on the strength of the double-layer repulsion, κ is the inverse screening length of the solvent, and D_i is the sum of the radii of the pair of interacting colloids.

$$U_e = \zeta \exp^{-\kappa(r-D_i/2)} \tag{2.1}$$

The lock-lock, lock-key and key-key repulsion strengths are chosen to be consistent with experimental zeta potential conditions.*Sacanna et al.* (2010) We summarize the interaction parameters in the Appendix.

The depletion interaction (U_d) between two spherical surfaces is modeled by:

$$U_d = -4\epsilon \left(\frac{\sigma}{r-\delta} \right)^{\alpha} \tag{2.2}$$

with ϵ the strength of the interaction, δ the interaction shift distance to the surface of the colloid, σ the range of interaction (Fig. 2.2b), and α the steepness of the well. The lock-lock, lock-key and key-key attraction strengths between different building blocks are chosen to match that of the depletion strengths listed in *Sacanna et al.* (2010), so that the net attraction energy is consistent with experiments, e.g. on the order of

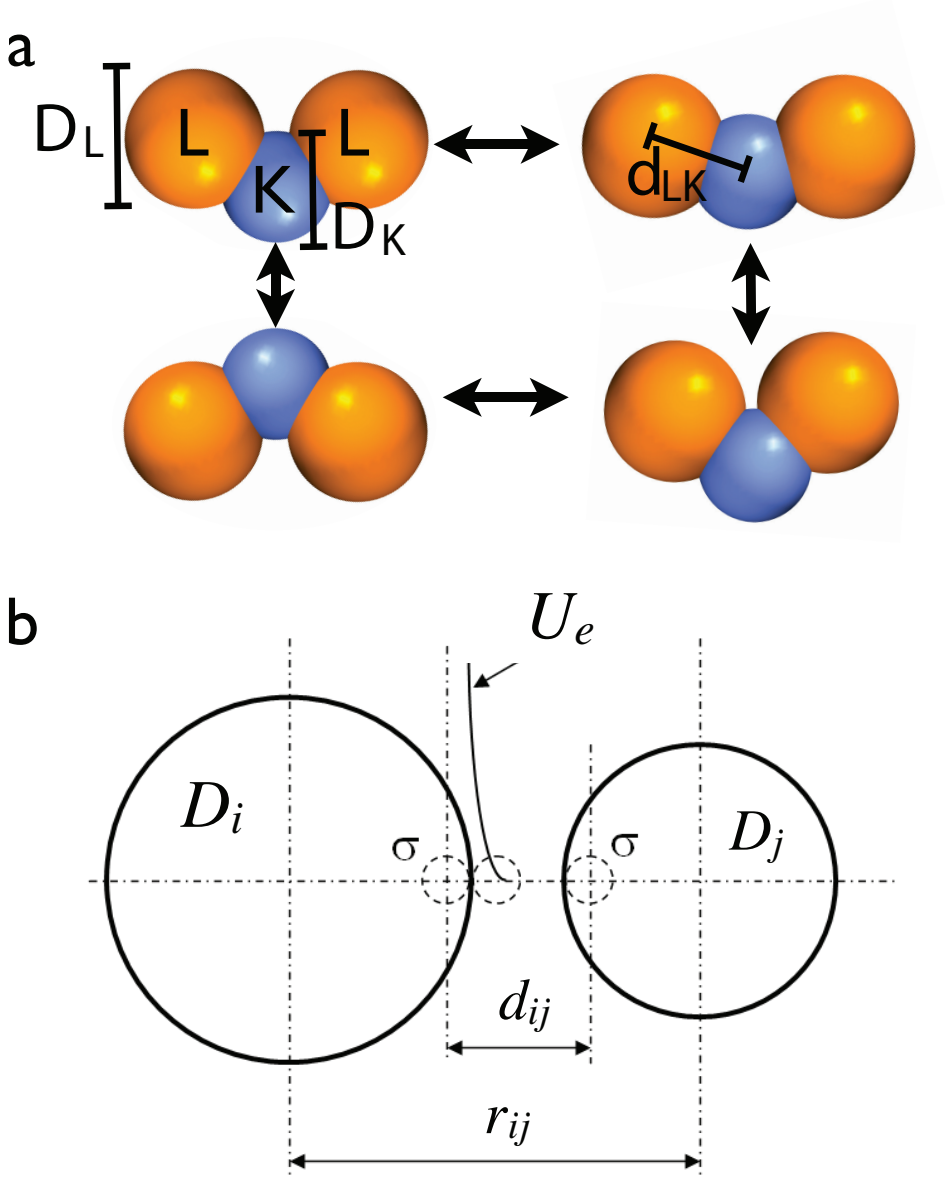

Figure 2.2: Model lock-and-key colloidal molecule with interactions is shown. The model lock-and-key building block is shown for two-lock building blocks with lock and key diameters D_L =1.3 and D_K =1.0, respectively (a). The bond length between the lock and key is shown to be d_{LK} =0.3. The reconfigurability of the building block is shown for four states. (b) The interactions between the building blocks can be broken down as pair interactions between two locks, two keys, and lock-key. The depletion attraction between the pair interacting colloids changes for different building block geometry.

1.0-2.0k_BT, which is considerably smaller than the lock-key depletion attraction.

For convenience, we express all quantities in dimensionless form, namely the distance $r = \bar{r}/\sigma_K$, time $\tau = \bar{t}\sqrt{D_K^2 m_K/k_BT}$, pressure $P = \bar{P}D_K^3/k_BT$, and energy $U = \bar{U}/k_BT$. . The mass of the beads is set to be $m_K = m_L = 1$ and the bonded locks are able to freely rotate with respect to each other as shown in Figure 2.2a. We consider the bond to be of zero mass and do not include lubrication forces in the lock cavity. We constrain the bond distance using a constrained molecular dynamics (MD) procedure similar to the SHAKE algorithm. *Ryckaert et al.* (1977)

We use hard interactions to investigate the role of shape. Hard interactions are purely repulsive excluded volume interactions, which allow us to isolate the role of entropy in the stabilization of observed crystal structures. The hard interaction model enforces excluded volume interactions between lock-lock, and key-key interactions. It is assumed that the bond between the lock-key is permanent, which is reasonable given the $10k_BT$ bond strength *Sacanna et al.* (2010), but permits a hinge-like motion.

2.3.1 Simulation Methods

We run both MD simulations in the NVT ensemble using a Langevin thermostat and NPT Monte Carlo simulations to assemble all the phases presented here. We construct the model building blocks and create a bond topology network to keep track of each lock-key bond. Periodic boundary conditions are used in the x-y plane. A typical run includes 10^6 time steps of athermal conditions for the building blocks to randomize the positions and orientations. Equilibration runs were achieved in 1-2*10^7 time steps.

For efficiency, Metropolis Monte Carlo simulation methods were utilized to generate the phase diagrams, while MD was used to check that each phase was kinetically achievable. The MC simulations include a pivot move to model the reconfigurability of the lock-key colloids. The reconfigurability move randomly samples a disk or sphere

of radius d_{LK} with a probability equal to standard rotation and translation moves. Again, the MC systems are initialized in athermal conditions, i.e. all interactions are purely repulsive, leading to a well-thermalized distribution of building blocks. In the NPT simulations, the box is gradually compressed or rescaled until crystallization is observed. To relieve defects, the box might be slightly expanded in a short time period, and then re-compressed. During the dilute simulations, we generate the condensed phase by rescaling the box until the packing density reaches 0.1-0.5 to facilitate the aggregation of the particles, then T is lowered into the coexistence region.

The simulated systems size varied from 500 to 9000 building blocks or 1000 to 45000 particles. Larger simulations were used to confirm that finite size effects do not affect the equilibrium structure. For certain cases, we performed independent simulation runs to ascertain that the resulting structures are reproducible, and not kinetically trapped states. The MD simulations were performed using HOOMD-Blue, our general-purpose open-source code optimized for graphics processing units *Anderson et al.* (2008); *Anderson and Glotzer* (2013), and LAMMPS *Plimpton* (1995). The Monte Carlo simulations were performed with in-house code.

2.4 Results

We present the representative results obtained from the range of the parameters that are readily accessible by the experimental conditions presented in *Sacanna et al.* (2010). The independent and combined effects of each of the five reconfigurability dimensions on the formation of the self-assembled structures are shown with an emphasis on assemblies with unique tilings and degeneracies. Because of the enormous parameter space, we choose to fix one parameter while varying the other in certain cases as indicated in the below subsections.

2.4.1 Geometric Phase Diagrams of Lock and Key Colloids Confined to a Plane

The assembled structures are organized into phase diagrams plotted as functions of N_L, D_L, and d_{LK}. Cross-sections of the phase diagram highlight essential features of the assembly of different colloidal molecules. We highlight the results for the N_L=1,2,3, and 4 colloidal molecules. We introduce a naming convention $L_C^N K_C$ where N = N_L, K the key sublattice, L the lock sublattice, and C is a shorthand for the crystalline sublattice.

We find that the lock-key distance is an important parameter in the crystallization of different crystal structures. The lock-key bond distance is defined as the amount of bond distance δ or nonadditivity*Dijkstra* (1998) between the lock-key particles. As δ increases, the deviation from regular additive colloidal spheres increases as well. We find that as the nonadditivity increases between the lock-key particles the ability for the system to order increases. (Figs 2.3,2.4) Furthermore, as the size ratio between the lock and key increases, the range of ordered structures increases. This phenomenon can be explained by the decreasing influence of the excluded volume of the key particle as the lock-key distance and size ratio increases. The excluded volume of the building block assembly takes on the shape of the combined excluded volume of the locks, which can readily self-assemble some of the crystal structures depicted in the phase diagram.

Another important factor in the stabilization of the assembled structures with small lock-key bond distance is the rotational free volume. We define the rotational free volume as the amount of free volume available for lock reconfigurability and use it as a simple model to describe steric hindrances to self-assembly at high volume fractions. Rotational free volume affects the self-assembly properties in a similar way to polydispersity. High polydispersity is known to act as a crystallization barrier for hard spheres.*Phan et al.* (1998) Similarly, high rotational free volume allows recon-

figurability to stabilize mixtures of shapes, which can inhibit crystallization. The continuum of shapes becomes incommensurate with any Bravais lattice and acts as a steric barrier to self-assembly. We find this phenomenon explains the large areas of disorder at small bond distance. (Figs. 2.3, 2.4) We find that the range of stability of reconfigurable colloidal molecules is much smaller then for rigid colloidal molecules. (Fig. 2.5) Crystal structures can form at smaller bond distances, but it implies that the configuration of the colloidal molecule has a large free energy gain. (Figs. 2.3,2.4)

At low lock-key distance, disordered aggregates compete with the crystal structures. These disordered aggregates (Dis) in Fig 2.3, 2.4, 2.5 have different characteristics depending on their location in the geometric phase diagram. General spherical codes *Phillips et al.* (2012) explain how the disordered aggregates local coordination changes with D_L and α.

$$2\pi = N_L \arcsin \frac{R_L}{R_L + R_K - \alpha} + (S - N_L) \arcsin \frac{R_L}{R_L + R_K} \tag{2.3}$$

Equation 2.3 describes how the local coordination of lock and key colloids changes with anisotropy dimensions. Equation 2.3 is a function of the number of locks N_L, radius of the key R_K and the radius of the lock R_L. The local coordination S is a highly nonlinear function of the size ratio and bond distance. The above equation is a simple geometric heuristic describing how aggregates of lock and key colloids change with geometric parameters. The nature of short-range order *Sheng et al.* (2006) in disordered aggregates could be elucidated by lock and key colloids. After this discussion, these disordered aggregates are grouped as one phase in the geometric phase diagrams.

2.4.1.1 Crystal Structures for the N_L=3 Colloidal Molecule

The colloidal molecule with N_L=3 self-assembles into five different crystal structures. Shown in Figure 2.3a is the geometric phase diagram between D_L and δ at fixed density and temperature. The cross-section is representative of the crystal structures observed in the larger D_L vs δ vs k_BT vs ω phase diagram. The phase diagram shows five different crystalline structures, which are $L^3_HK_{DH}$, $L^3_{ET}K_R$, $L^3_{PTS}K_R$, $L^3_{EH}K_R$, and $L^3_{ATS}K_R$ (Fig. 2.3b-f). Notably, the disordered quasicrystal $L^3_{ATS}K_R$ is reminiscent of the dodecagonal triangle square quasicrystals, and the $L^3_{PTS}K_R$ and $L^3_{EH}K_R$ crystal structures are observed, to our knowledge, for the first time. The latter two structures, as characterized below, have the complexity of alloys but are assembled with surprisingly simple design rules.

At larger bond distances ($\delta > 0.3$), the N_L=3 molecular colloid self-assembles the $L^3_HK_{DH}$ crystal structure. (Fig. 2.3b) In the $L^3_HK_{DH}$ crystal structure, the locks form a hexagonal sublattice and the keys form a frustrated sublattice. By increasing the δ between lock and key, the effective excluded volume of the key decreases, and triangular trimers are free to self-assemble without steric hindrance. The assembly of the $L^3_HK_{DH}$ is not unexpected since hard trimers form an aperiodic hexagonal crystal. *Kowalik and Wojciechowski* (2005) The aperiodicity of the locks is due to the keys being at the center of the molecule. Aperiodic crystals of hard trimers have negative Poisson ratios *Kowalik and Wojciechowski* (2005), implying that minor changes in the geometry of the molecular colloid such as changing the bond distance from δ=0.3 to δ=0.25 at D_L =1.7 (Fig. 2.3) could have a dramatic effect on the mechanical properties of assemblies.

At large bond distance ($\delta > 0.3$) and small size ratio (D_L=1.2) the N_L=3 colloidal molecule self-assembles the $L^3_{ET}K_R$ crystal structure. (Fig. 2.3d) The elongated triangular (ET) lock tiling in the $L^3_{ET}K_R$ crystal structure occurs in different alloys as a cross-section of TlI *O'Keeffe and Hyde* (1980), which is used to improve the

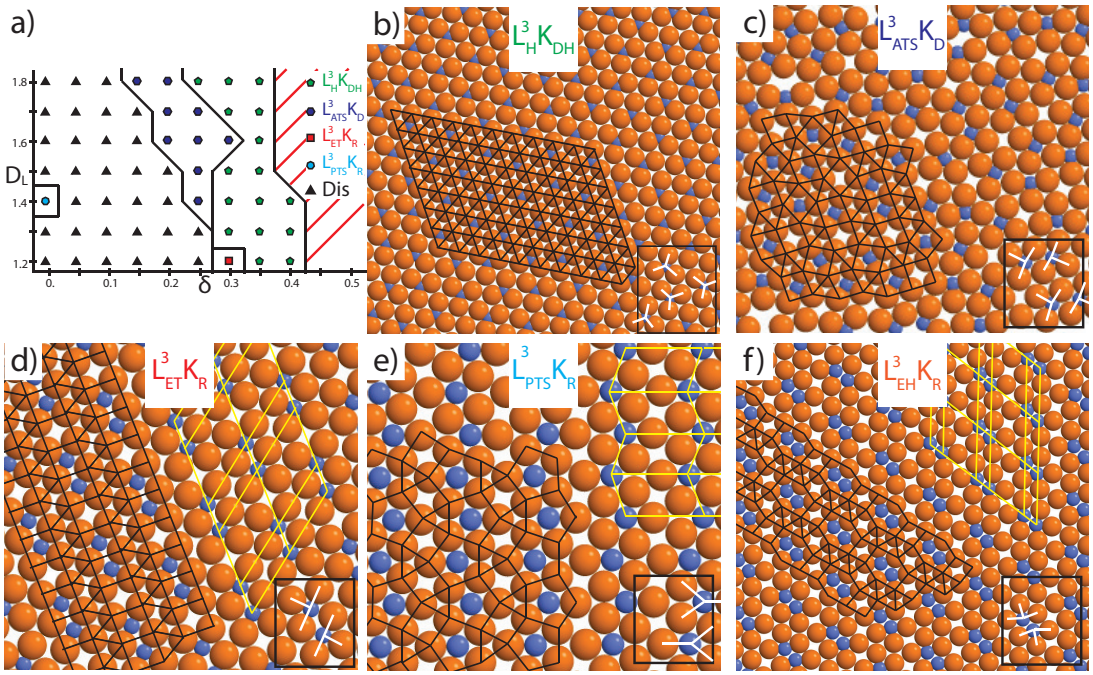

Figure 2.3: Phase diagram for N_L=3 particle showing stability regions as a function of size ratio (D_L where D_K=1), and bond distance (δ). A representative slice of the phase diagram is shown above along with all crystal structures observed. For each crystal, the inset highlights the configuration of the molecular colloids (white). We show the vertex configurations of the lock (black) and keys (yellow). A representative snapshot of each crystal structure is shown. The crystalline structures observed for N_L=3 are the triangular degenerate crystalline with a hexagonal lock tiling, and a disordered key lattice ($L^3_H K_{DH}$) (b), a random triangle, square lock tiling with disordered keys at D_L=1.7, δ =0.2 ($L^3_{ATS} K_D$.) (c).the Archimedean elongated triangular lock tiling ($3^3, 4^2$) with a binary rhombus key tiling keys at D_L=1.8, δ =0.05 ($L^3_{ET} K_R$) (d), a (3.4.5.4, $(3.4.5^2)^2$) lock tiling with an alternating rhombus key tiling keys at D_L=1.3, δ =0.05 ($L^3_{PTS} K_R$) (e), an elongated hexagon, square, triangle lock tiling with a binary rhombus key tiling at D_L =1.6,δ =0.25 ($L^3_{EH} K_R$) (f).

performance of mercury lamps. *REILING* (1964) The ET Archimedean tiling is observed in the binary nanoparticle superlattices of Au and Fe colloids. *Talapin et al.* (2009) The ubiquity of the ET tilings in soft and hard matter systems makes their discovery in molecular colloids less surprising. The key sublattice lies on the projected Tl sublattice with systematic vacancies, and the lock sublattice lies on the I sublattice. The lock sublattice for the $L^3_{ET}K_R$ crystal structure is the same as $L^4_{ET}K_R$, crystal structure (Fig. 2.6), but the key sub lattice of $L^3_{ET}K_R$ has fewer systematic defects than $L^4_{ET}K_R$.

At intermediate size ratio D_L=1.4 and low bond distance ($\delta < 0.05$), the N_L=3 colloidal molecule self-assembles the $L^3_{PTS}K_R$ crystal structure (Fig. 2.3e). The $L^3_{PTS}K_R$ crystal structure has a (3.4.5.4, $(3.4.5^2)^2$) lock sublattice and a rhombic key sublattice. The (3.4.5.4, $(3.4.5^2)^2$) tiling is characteristic of a cross-section of the UVO_5 crystal structure *Dickens et al.* (1992); the key sublattice lies on the projected uranium atomic positions, the lock sublattice lies on the oxygen atomic positions, and the V atoms are vacant. *Dickens et al.* (1992) Mixed oxides of uranium with transition metals (V, Ti) can be used as intercalation compounds for small cations. *Dickens et al.* (1993) The $L^3_{PTS}K_R$ crystal structure has a structure similar to known intercalation materials (UVO_5), which implies that layers of this colloidal crystal could be useful for energy storage materials, but a more through study would need to be done on the thermodynamics and kinetics of diffusion of ions through the material.

At large size ratio D_L >1.3, and intermediate bond distance $\delta = 0.15 - 0.3$, a random triangle square lock sublattice and a disordered key sublattice form ($L^3_{ATS}K_D$). (Fig. 2.3c) Random triangle square tilings occur in disordered dodecagonal quasicrystals, such as $Ta_{1.6}Te_{.34}$. *Krumeich et al.* (1998) Unlike in normal triangle square dodecagonal quasicrystals, the disordered dodecagonal quasicrystals have a square triangle ratio that has a small deviation from the perfect square triangle ratio of the perfect quasicrystal. *Krumeich et al.* (1998); *Stampfli* (1986) Since dodecagonal qua-

sicrystals and certain classes of hyperuniform disordered points sets have complete photonic band gaps *Florescu et al.* (2009); *Zachary and Torquato* (2009), disordered dodecagonal quasicrystals are expected to have interesting photonic properties.

At small bond distance ($0.05 < \delta < 0.2$) and intermediate size ratio D_L=1.4 and lower k_BT, the N_L=3 colloidal molecule self-assembles the $L^3_{EH}K_R$ crystal structure. (Fig. 2.3f) The $L^3_{EH}K_R$ crystal structure has an elongated hexagon square triangle (3.4.6.4, 3^2.4.6, 3^3.4.6) lock sublattice, and rhombic key sublattice ($L^3_{EH}K_R$). The lock sublattice is related to the Archimedean rhombitrihexagonal tiling (3.4.6.4) by elongating the hexagon along its apothem. Elongated hexagons occur in projections of complex metal alloys, such As Ti-Al-Mn-Pd *Heggen et al.* (2010) along the [010] direction and have been predicted to occur in binary hard sphere systems using genetic algorithms. *Filion and Dijkstra* (2009) To our knowledge, the crystal structure $L^3_{EH}K_R$ has analogues in complex metal alloys, but no known material systems reproduce this crystal structure exactly.

2.4.1.2 Crystal Structures for the N_L=2 Colloidal Molecule

The lock-and-key colloids with N_L=2 self-assemble into nine different crystal structures. We show a geometric phase diagram for the size ratio (D_L with D_K=1) and bond distance δ, at fixed density ϕ and temperature. (Fig. 2.4a) Two of the nine crystal structures are unexpected random crystals and several are characteristic of complex metal alloys. All of these crystal structures are accessible by tuning the bond distance and size ratio of the N_L=2 colloidal molecule. (Figs. 2.4,2.5)

At both high and intermediate values of lock-key bond distance ($\delta = 0.3-0.5$), the N_L=2 colloidal molecule forms the $L^2_HK_K$ crystal. (Fig. 2.4b) In the $L^2_HK_K$ crystal structure, the locks form a triangular sublattice and the keys lie on a fractionally filled kagome sublattice (see *Kohlstedt and Glotzer* (2013) for more detail of the kagome phase). The fractionally filled degenerate kagome key sublattice ($L^2_HK_K$) has

been observed in frustrated spin systems *Rüegg and Fiete* (2011) and colloids with highly directional interactions. *Chen et al.* (2011) The assembly of the $L_H^2K_K$ is not surprising since the center of mass, which is where the keys lie, of hard dimers are known to lie on the Kagome lattice. *Wojciechowski* (1992) The aperiodic crystal of dimers is known to have a negative Poisson ratio. *Kowalik and Wojciechowski* (2005)

At high bond distance δ=.45 and $D_L = 1.2$, the N_L=2 colloidal molecule forms the $L_{ET}^2K_R$ crystal structure. (Fig. 2.4b) The locks form a sheared Archimedean elongated triangular ($3^3.4^2$) sublattice, and the keys form a rhombic sublattice ($L_{ET}^2K_R$). (Fig. 2.4b) The sheared Archimedean tiling is an intermediate tiling between the elongated triangular ($3^3.4^2$) and the triangular (3^6) tiling. By increasing the size ratio to $D_L = 1.3$, we can transform the $L_{ET}^2K_R$ into the triangular $L_H^2K_K$. It is interesting to note that this transformation, with respect to the lock sublattice, corresponds approximately to the transformation between rutile and monoclinic zirconia. *O'Keeffe and Hyde* (1980)

At high bond distance ($\delta = 0.45$) and high size ratio (D_L=1.8), the N_L=2 colloidal molecule forms the $L_H^2K_D$ crystal structure. (Fig. 2.4d) In the $L_H^2K_D$ crystal structure, the locks form a triangular sublattice, and the keys are disordered. The proximity of the $L_H^2K_D$ and $L_H^2K_K$ crystal structures on the phase diagram motivates the altering of the bond distance (from δ=0.45 to δ=0.4 at D_L =1.7) (Fig. 2.3) to switch between assemblies of a partially ordered crystal ($L_H^2K_D$) to a perfect crystal ($L_H^2K_K$).

At high bond distance ($\delta = 0.4-0.45$) and high size ratio (D_L=1.5-1.8), the N_L=2 colloidal molecule forms the $L_{TS}^2K_R$ crystal structure. (Fig. 2.4e). In the $L_{TS}^2K_R$ crystal structure, the locks form a $(3^2.4^2.3, (3^3, 4^2)^3)$ triangle square lock sublattice and a rhombic key sublattice. The lock sublattice is a 4-uniform tiling, meaning it is an edge-edge tiling made of regular polygons with four different vertex configurations. To our knowledge, the crystal structure observed has no known material equivalent.

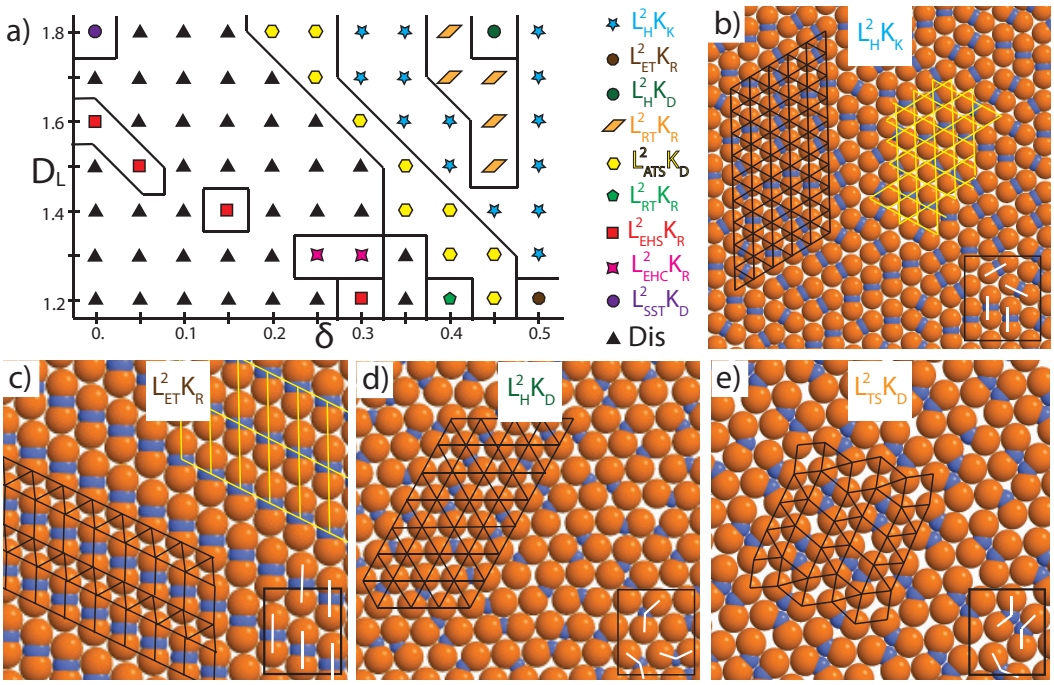

Figure 2.4: The geometric phase space for N_L=2 molecular colloid is shown above. For each crystal, the inset highlights the configuration of the molecular colloids (white). We show the vertex configurations of the lock (black) and keys (green). A representative snapshot is shown of each crystal structure. We show a cross-section at fixed density (σ=.7) as a function of the geometric parameters size ratio (D_L where D_K=1) and bond distance (α). The crystal structures for N_L=2 are a hexagonal lock tiling and a substitutionally disordered kagome key tiling ($L^2_HK_K$), (b) a sheared Archimedean elongated triangular lock tiling ($3^3, 4^2$) and a rhombic key tiling at D_L=1.2, α =0.5 ($L^2_{ET}K_R$) (c), a hexagonal lock tiling and a disordered key tiling ($L^2_HK_D$), (d) and ($3^2.4^2.3, (3^3, 4^2)3$) triangle square tiling at D_L=1.5, α =0.45 ($L^2_{TS}K_D$) (e).

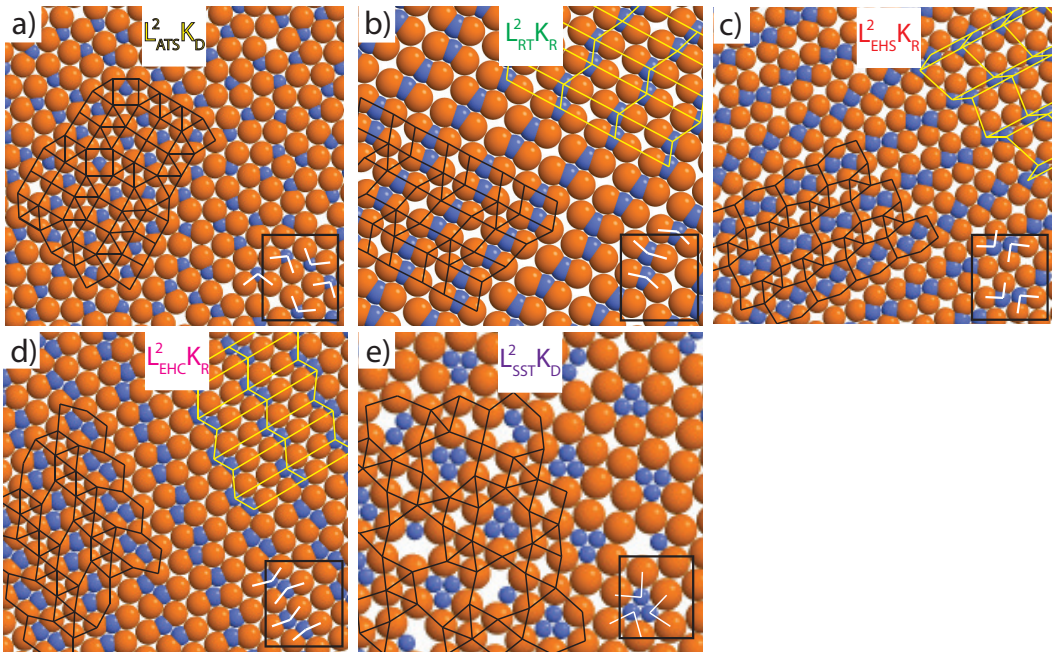

Figure 2.5: We highlight the crystal structures at low α for the N_L=2 molecular colloid above. The crystal structures for N_L=2 are at D_L=1.2, α =0.5 ($L^2_{ATS}K_D$) (a), a binary rhombic lock tiling with a binary rhombic key tiling ($L^2_{RT}K_R$) at D_L=1.2, α =0.4 (b), an elongated hexagon triangle square lock tiling with a binary rhombic key tiling at D_L=1.2, α =0.5 and σ=.3 ($L^2_{EHS}K_R$) (c)an elongated hexagon chain triangle tiling at D_L=1.3, α =0.3 ($L^2_{EHC}K_R$) ,(d) and a shield square triangle tiling at D_L=1.7, α =0.05 and ($L^2_{SST}K_D$) (e).

At intermediate bond distance ($\delta = 0.2 - 0.4$) , the N_L=2 colloidal molecules form the $L^2_{ATS}K_D$ crystal structure. (Fig. 2.5a) The $L^2_{ATS}K_D$ crystal structure has a random triangle square lock sublattice and a disordered key sublattice. The random triangle square tiling $L^2_{ATS}K_D$ is similar to the$L^3_{ATS}K_D$ except that the density of the keys is much higher due to the lock number. The triangle square ratios in the disordered quasicrystals are different between $L^2_{ATS}K_D$ and $L^3_{ATS}K_D$ due to the lock number. It is interesting that both $L^2_{ATS}K_D$ and $L^3_{ATS}K_D$ reside on the geometric phase diagram between disorder and a hexagonal crystal $L^3_HK_{DH}$ and $L^2_HK_K$(Figs 2.3,2.4). The random crystal structure arises from the geometry of the particle (smaller α) and the reconfigurability from the increased rotational free volume destabilizing the hexagonal crystal.

At small size ratio ($D_L = 1.2$), the $L^2_{RT}K_R$ crystal structure forms (Fig. 2.5b) with the locks occupying a triangle rhomb sublattice and keys a rhombic sublattice. To our knowledge, neither the $L^2_{TS}K_R$ and $L^2_{RT}K_R$ crystal structures observed have known material equivalents.

The disordered region of the phase diagram competes with the $L^2_{EHS}K_R$ crystal structure. The $L^2_{EHS}K_R$ crystal structure has an elongated hexagon square triangle lock sublattice and a rhombic key sublattice ($L^2_{EHS}K_R$). (Fig. 2.5c) The $L^2_{EHS}K_R$ is related to the 2-uniform (3.6.3.6, $(3^2.6^2)^2$), or the β-W net *O'Keeffe and Hyde* (1980), by elongating the hexagon along the shared apothem between neighboring hexagons. The β-W net, which exists in the Cr_3Si crystal structure, was found in experiments of oppositely charge colloids.*Hynninen et al.* (2006)

The disordered region of the phase diagram also competes with the $L^2_{EHC}K_R$ crystal structure. (Fig. 2.5d) The $L^2_{EHC}K_R$ crystal structure has an elongated hexagon triangle lock sublattice and a rhombic key sublattice. The tiling is related to the β-W net, and the elongation occurs along the hexagon apothem in the direction of the triangle. It is interesting to note that two different elongated hexagonal crystals

$L^2_{EHC}K_R$ and $L^2_{EHS}K_R$ are proximal on the phase diagram. By increasing the size ratio to $D_L = 1.3$, we can transform the $L^2_{EHS}K_R$ into the triangular $L^2_{EHC}K_R$. The implication is that two crystal structures characteristic of complex metal alloys can be toggled by a simple geometric parameter.

At small bond distance ($\delta = 0.0$) and high size ratio, the N_L=2 colloidal molecule forms the $L^2_{SST}K_D$ crystal structure. (Fig. 2.5e) In the $L^2_{SST}K_D$ crystal structure, the lock forms a random shield triangle square sublattice, and the locks are disordered. A dodecagonal quasicrystal, the shield tiling *Grünbaum and Shephard*, closely related to the aperiodic shield triangle square lock sublattice, is potentially applicable to photonic band gap materials. *Man et al.* (2005)

2.4.1.3 Crystal Structures for the N_L=1,4 Colloidal Molecule

Figure 2.6 shows the geometric phase diagrams obtained for lock-and-key building blocks of N_L = 1,4 confined in 2D. The phase diagrams depicted in Figure 2.6 show the crystal structures found as one varies D_L and the bond distance δ, which is related to d_{LK} by $2\delta = 1 + D_L - 2d_{LK}$, for each lock in the building block.

Far from $D_L = 1$ and at large bond distance ($\delta \approx 0.40$) a frustrated hexagonal phase, ($L^1_H K_D$), that is similar to frustrated dipoles confined to a triangular lattice *Greedan* (2001), forms for the $N_L = 1$ building block (Figs. 2.6a, 2.6b). In the $L^1_H K_D$ phase, the locks form a frustrated hexagonal sublattice, and the keys are disordered. In the limit of complete bond distance, where the key particle completely overlaps the lock particle, the frustration diminishes, and a hexagonal lattice emerges ($\delta \gg 0.5$). Thus, the single lock acts as a steric hindrance to the assembly of a hexagonal lattice.

For the N_L =4 colloidal molecule, the Archimedean elongated triangular tiling is observed at large δ. At $\delta \approx 0.15$, a crystal structure ($L^4_{ET}K_R$) forms with the locks on an Archimedean elongated triangular ($3^3.4^2$) sublattice and the keys on a rhombic sublattice (Fig. 2.6d). The $L^4_{ET}K_R$ structure is entropically stabilized by the shape

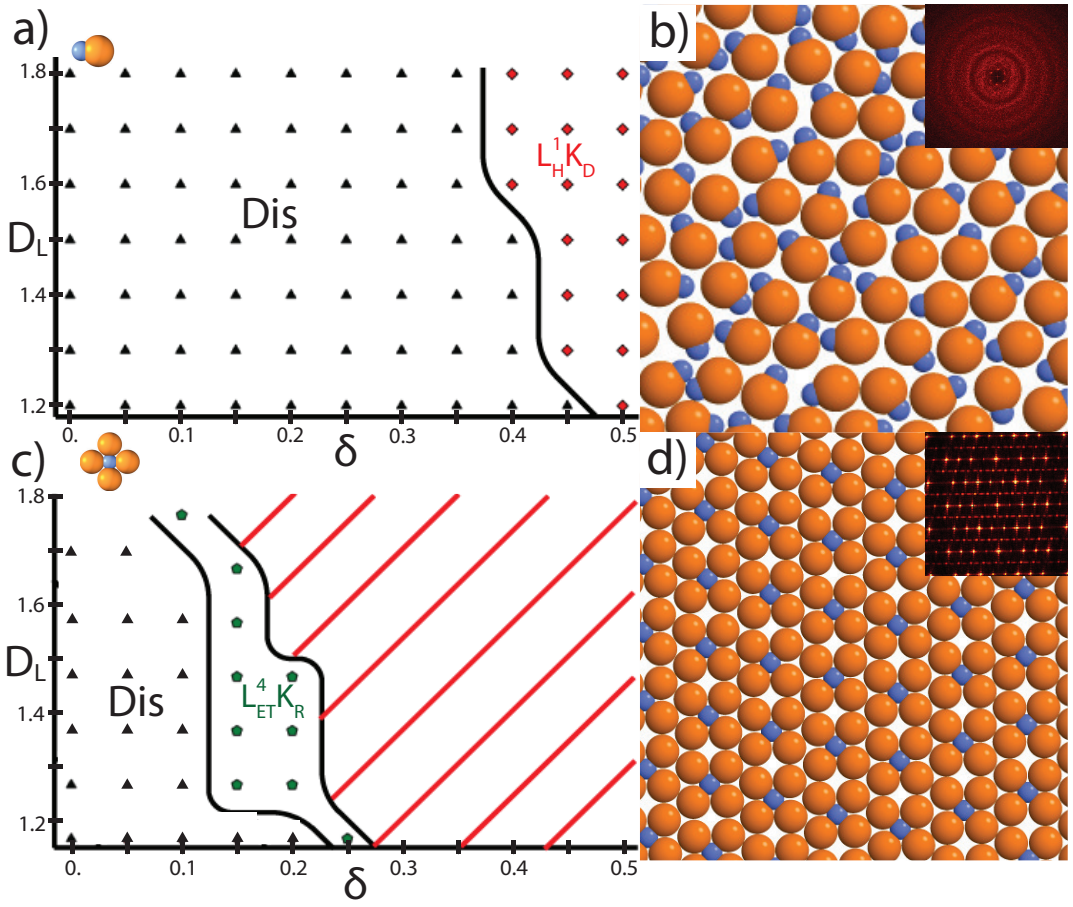

Figure 2.6: The geometric phase space of the clusters is summarized as phase diagrams of D_L and δ for (a) one- (and (c) four-lock particles. Each phase diagram is a slice of phase space at constant density. In the one-lock cluster (a) we show a large frustrated/glassy (Dis) assembly that with increasing overlap transforms into a partially ordered hcp phase ($L_H^1K_D$). (h) Four-lock clusters assemble into rhombic lattice ($L_{ET}^4K_R$) from a small Dis phase via rhombic partially ordered phase ($L_D^4K_R$). Geometrically inaccessible regions arise for N_L=4 and are shown as red diagonals. Representative snapshots for the two observed crystalline phases in the phase diagrams are shown. Additionally, we show the spacing and symmetry of the phases with the diffraction pattern for each structure. In the one-lock case (a) we show the $L_H^1K_D$ crystal structure for D_L=1.8, δ =0.5(b). In the four lock case (d), we show the and $L_{ET}^4K_R$ crystal structure at D_L=1.6, δ =0.15.

of the building block.

2.4.2 Reconfigurability and Assembly

The lock mobility γ_r determines the shape-shifting rate of the lock-key assemblies. By increasing the lock mobility, building blocks sample a continuum of shapes at a faster rate. We explore how hinge-like reconfigurability in the $N_L = 2$ building block affects the stability of a partially ordered crystal structure ($L_H^2 K_D$) as a function of bond length and size ratio. We find that, as a function of bond length, the stability region for the $L_H^2 K_D$ crystal structure is smaller for the reconfigurable building block than the rigid building block. This variable stability region controlled by reconfigurability opens opportunities for finely controlled rate-dependent crystal-disorder transformations.

Lock mobility γ_r changes the stability range of the crystal structures. For a given size ratio D_L, increasing the bond length δ causes the rotational free volume to increase. We focus on the two-lock building blocks as a representative case. We choose a well-ordered $L_H^2 K_D$ structure for a given value of D_L as the reference crystal structure and calculate a shape-matching order parameter with respect to assembled equilibrium crystal structures as a function of building block geometric parameters (D_L, δ). Because the locks lie on a hexagonal lattice in the $L_H^2 K_D$ crystal structure, it is natural to use the six-neighbour bond order parameter σ_6 as our shape matching criterion. *Keys et al.* (2011) The order parameter σ_6 is unity if the crystal structure is a perfect hexagonal lattice. For both building blocks, the stability region (the geometric state points such that $\sigma_6 > 0.95$ highlighted in grey) is determined by the locks ability to efficiently nest for a given D_L. For both building blocks, the cutoff for good assemblers ($\sigma_6 > 0.95$) is shifted to higher values of δ as the size ratio D_L increases.(Fig. 2.6a,b) Outside of this stability range, the lock mobility stabilizes an amorphous solid (Dis).

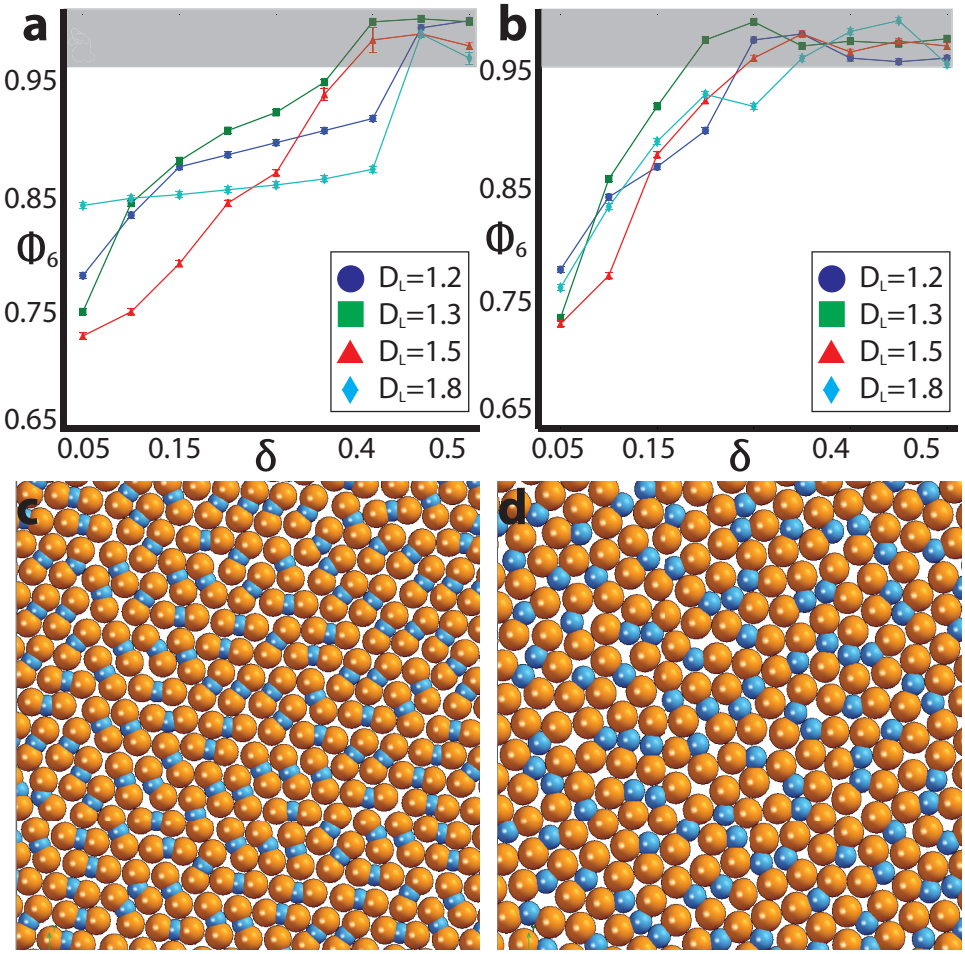

Figure 2.7: We highlight the effect of reconfigurability on the stability of crystalline structures for the $N_L = 2$ building block. An HCP shape matching order parameter σ_6 is used as a function of bond length d_{LK} for different lock-key sizes (D_L). Each curve is obtained by averaging across several independent runs. Error bars are smaller than the marker size. We compare the order parameter behavior for (a) locks that are able to move around the key and for (b) rigid building blocks fixed in a linear trimer geometry. (c) We show representative shapshot of a good assembler with order parameter $\sigma_6 = 0.97$ and d_{LK}=.75 and D_L=1.33. (d) Also, a representative snapshot for a poor assembler is shown with order parameter $\sigma_6 = 0.83$ and d_{LK}=1. and D_L=1.33

For the reconfigurable building block, the rotational free volume of the locks allows the lock mobility to cause additional packing frustration between lock and keys. By comparing the reconfigurable building block to the rigid building block, we can understand the role that lock mobility plays in the stabilization of the $L_H^2K_D$. Because the building blocks adopt a linear shape in a $L_H^2K_D$ phase (Fig. 2.3d), we use rigid linear particles for the rigid case. Figure 2.7 shows the σ_6 order parameter for reconfigurable and rigid particles as a function of D_L and δ. Comparing the σ_6 order parameter in Figure 2.4b with that in Figure 2.4a, we observe a similar behaviour, i.e. there is an optimal range of δ for each value of size ratio D_L in which the locks form an ordered $L_H^2K_D$ structure. For the rigid building blocks, the optimal range is broadened towards higher values of d_{LK} for a given value of D_L. For example, the rigid D_L=1.3 building block assembles into a $L_H^2K_D$ structure for $\delta > 0.2$. The reconfigurable building blocks can retain the $L_H^2K_D$ structure only up to $\delta = 0.4$. (Fig. 2.7a,b) The broadened stability range of rigid particles suggests that lock mobility promotes local packing frustration and steric barriers for assemblies at high density and pressure. Small kinks in the yield are expected since the rotational free volume changes with geometric parameters, which subtly affects the crystalline yield. The majority of the kinks arise in the stability region of the $L_H^2K_D$ crystal structure, highlighting how certain geometric state points have favourable kinetics. One can imagine using the lock mobility, or toggling the bond distance between the locks and key, to directly reconfigure between crystalline and disordered states to change the mechanical properties of the assembly.

2.4.3 Lock and Key Colloids in quasi-3D

We extend the spatial confinement from 2-D to quasi-3D, where the keys are still confined in the x-y plane, but now the locks are able to rotate out of the plane. The quasi-3D confinement reproduces the experimental conditions where the particles can

move within a thin film or on a substrate without diffusing normal to the surface. In order for the out of plane rotations to be unconstrained, the periodic boundary conditions are only applied to x- and y-directions.

By changing the confinement characteristics from 2D to quasi-3D, we show how frustrated crystal structures in 2D can order in quasi-3D. In quasi-3D, the crystal structures can either resemble the crystal structures observed in 2D (Fig. 2.8), or take on characteristics that are fundamentally different. (Figs. 2.8,2.9) We then focus on the cases where the assembled structures are fundamentally different from 2D assembly.

In 2D, there are regions of the geometric phase diagram that are disallowed for $N_L = 3$ and $N_L = 4$. (Fig. 2.4,2.5,2.6) Considering these geometric state points in quasi-3D would demonstrate how altering the confinement characteristics affects the assembled structures. For instance, the $N_L = 4$ building blocks can locally relax into tetrahedral coordination. The results for $N_L = 4$ outside the permitted 2-D geometrical confinement with $D_L = 1.33$ and $d_{LK} = 0.75$ are shown in Figure 2.6. This geometry provides us with a model tetrahedron, as the locks cannot all become coplanar. We observe an interesting ABC stacking where three layers emerge with a key layer sandwiched between two lock layers. The top and bottom lock layers form a square lattice S offset from each so that the top layer is in the interstitials of the bottom layer. The middle layer of keys then lies on a hexagonal lattice H shown in Figure 2.8a (blue and orange, respectively). The monolayer is shown from perspective in Figure 2.5b to show the offset lock layers ($L_H^4 K_S$). The structure is similar to the zinc blende structure seen in binary alloys. *Barrett and Massalski* (1966) The long-range nature of the lattice is revealed by the 2D diffraction image taken along (001) plane as shown in Figure 2.8c. Regions of phase space inaccessible in 2D due to geometric constraints can form crystalline structures such as tetrahedrally coordinated monolayers.

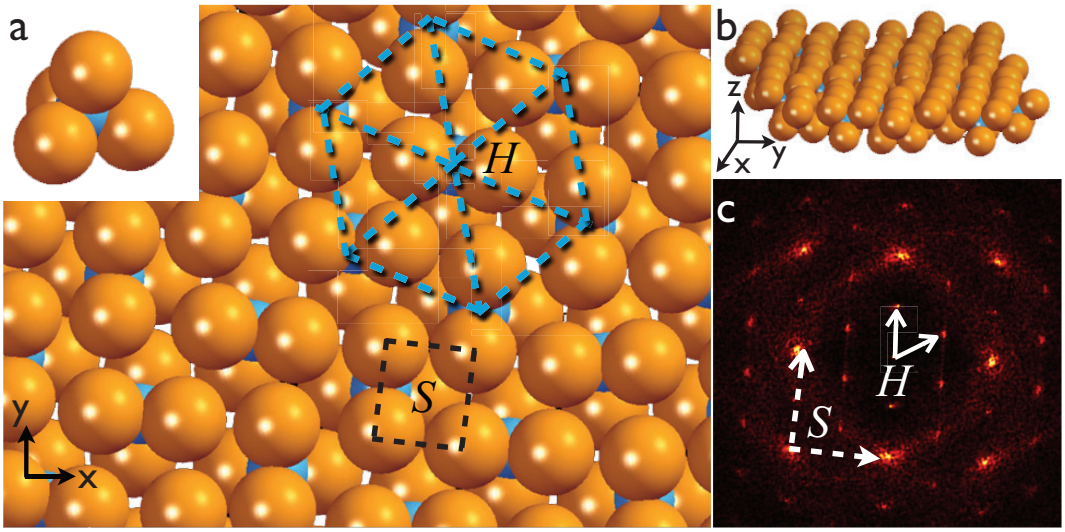

Figure 2.8: Assembled tetragonal monolayer from four-lock clusters with quasi-3D confinement. The cluster geometry is $D_L = 1.33$ and $d_{LK} = 0.75$. The clusters form an ABC stacked layer with the locks forming a square lattice on the top and bottom layers (a), while the keys form a hexagonal lattice. We allow the monolayer of locks to freely rotate in the z-direction (b). The 2-D diffraction image shows the four-fold square symmetry of the locks and the six-fold hexagonal symmetry of the keys while looking down (001) plane (c).

In regions that are shared in both 2D and quasi-3D, we take a collection of geometric state points (Table A2) from the $N_L = 1$ phase diagram (Fig. 2.7a) and change the confinement from 2-D to quasi-3D. We find that the $N_L = 1$ building block in 2D can self-assemble a frustrated hexagonal crystal structure ($L_H^1 K_D$) and a disordered phase. (Fig. 2.4a). We observe a crystalline monolayer isostructural to PbO in the region of frustrated Hp region.($L_T^1 K_S$). The PbO crystal structure consists of three layers of lock and keys. (Fig. 2.8a) The building blocks align into two rows with antiparallel orientation. The top and bottom layer of locks form a square lattice, while the key middle layer forms a square lattice with different lattice spacing (Fig. 2.9b). By changing the confinement characteristics of $N_L = 1$, we can switch between a $L_T^1 K_S$ crystal and a frustrated $L_H^1 K_D$ phase. (Fig. 2.9a,b) The $N_L = 1$ building block is representative of a building block that is sensitive to the confinement characteristics of the assembly.

For the $N_L = 2$ building block, confinement does not dramatically change the crystal structure. At geometric state points where the $L_H^2 K_K$ and $L_H^2 K_D$ are stable (Table S2), changing the confinement stabilizes a $L_{HH}^2 K_D$ crystal structure. $L_{HH}^2 K_D$ crystal structure contains two hexagonal layers with a disordered key layer in between. (Fig. 2.9a) The $L_{HH}^2 K_D$ crystal structure resembles the lock $L_H^2 K_D$ crystal structure in that both crystal structures have locks arranged with hexagonal order and keys that are disordered. (Fig. 2.5d, 2.9b) Spatial confinement in shared regions of the geometric phase diagram can lead to transitions where the both crystal structures are similar ($L_H^2 K_D$-$L_{HH}^2 K_D$), or whose structurally characteristics are unrelated ($L_H^1 K_D$-$L_T^1 K_S$).

2.4.4 Reconfigurable Crystals

Binary nanoparticle superlattices *Talapin et al.* (2009); *Shevchenko et al.* (2006) (BNSL) are promising materials for their electronic *Urban et al.* (2007) magnetic

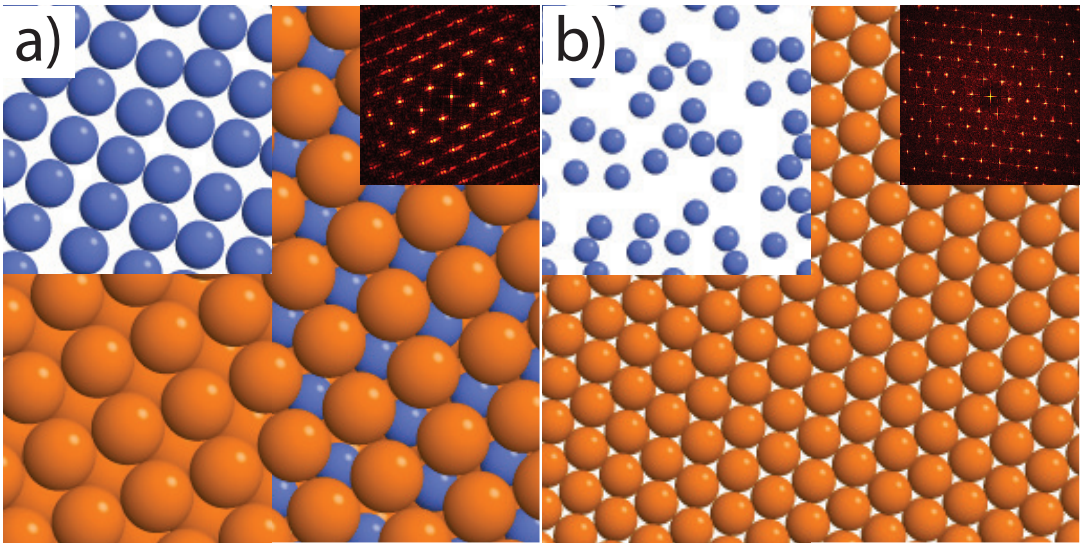

Figure 2.9: The effect of confinement on 2-lock and 1-lock clusters is summarized above. Representative snapshots of crystal structures under quasi-3D confinement are shown above (a,b). The inset for quasi-3D confinement show both lock and keys in the right half, only locks in the top left, and only keys in the bottom left. We show the diffraction pattern for each representative snapshots. For the one-lock case, the 2 quasi-3D crystal structure $L_T^1 K_S$ is shown for D_L=1.7, δ =0.5(a). For the two-lock case, the quasi-3D crystal structure $L_{HH}^2 K_D$ is shown for D_L=1.5, δ =0.5(b).

Cheon et al. (2006) and fluorescence *Shevchenko et al.* (2008) properties. We expand upon previous work on BNSL by reporting the self-assembly of a switchable BNSL (SBNSL), which toggles between a binary mixture and a partially ordered crystal with alternating layers of order and disorder. Changing the effective bond length or the size ratio of the reconfigurable molecular molecules toggles the SBNSL structures. Although DNA has been used to switch between two different BNSL *Maye et al.* (2010), we show that through shape change via reconfigurability dimensions we can toggle between a BNSL and a partially ordered binary nanoparticle crystal. Through shape change, the tetrahedral coordination of a BNSL becomes frustrated, which leads to the stabilization of partially ordered structures. The ability to design molecular switches with dual material properties, such as surface plasmon resonance, *Podsiadlo et al.* (2010) opens up a great opportunity for the development of multifunctional nanomaterials. Colloidal molecules that stabilize BNSL with crystal-crystal transformations could be used in photonic, optical, and sensor applications.

Switchable binary nanoparticle superlattices use the reconfigurability dimensions of the lock-and-key colloidal molecules to influence the thermodynamic equilibrium structure. We investigated the effect of the bond length and size ratio on the tetrahedrally coordinated $N_L = 4$ case to understand how this coordination can be distorted by shape change to stabilize partially ordered structures in the presence of spatial confinement, i.e. in quasi-3D. In principle, the distortion of the quasi-3D tetrahedrally coordinated building block is similar to the high packing fraction crystal transitions ($L_H^2 K_D \rightarrow L_H^2 K_K$) where a sublattice disorders by changing the size ratio and bond distance (Fig. 2.4) Indeed, the changes in the bond length or size ratio to give rise to structural transformations (Fig. 2.10a-c) The base radius ratio and bond length leave the locks rigid and inhibit the excluded volume of the key from affecting the assembly of colloids. By transforming the size ratio, or bond length, we alter the relative importance of the excluded volume of the key in comparison to the lock and

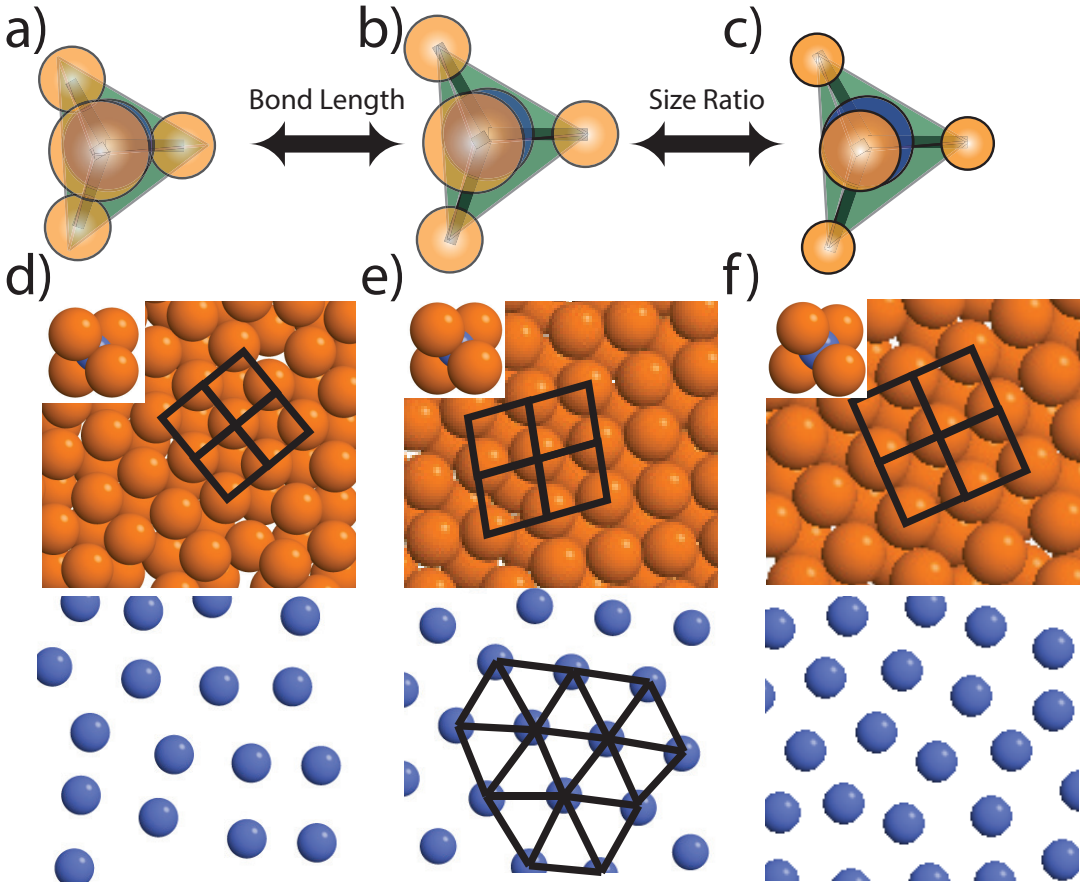

Figure 2.10: Schematic of quasi-3D partially ordered crystal-crystal transformation using molecular colloids reconfigurability dimensions and representative snapshots of the transformation are shown above. Tuning the size ratio or bond length of the tetrahedrally coordinated molecular colloid act as geometric knobs that distort the assembly of a crystalline structure.(a-c) By transforming the cluster geometry from $d_{LK} = 0.75$ to $d_{LK} = 0.80$ at $D_L = 1.33$, we can transform the crystal structure from an ABC stacked layer of with four fold symmetric locks, and six fold symmetric keys (e) (See Figure 6) into a system where locks preserve their four fold order, but the keys are disordered(d). By changing the size ratio from $D_L = 1.33$ to $D_L = 1.18$(f), we can reproduce the same crystal structure transformation above, but through a different mechanism.

stabilize different structures. The transformations distort the tetrahedral coordination of the locks and keys, facilitating two possible crystal-crystal transformations. The first crystal structure transformation converts a hexagonal monolayer sublattice of locks with a square monolayer sublattice of keys ($L_H^4 K_S$) to a hexagonal monolayer sublattice of locks with a disordered sublattice of keys ($L_H^4 K_D$). (Fig. 2.10d-e). The proximity of the two state points lends itself to switchable materials due to the small change (7%) in bond length needed to activate the transition. The second transformation converts the $L_H^4 K_S$ structure with $D_L = 1.33$ and $d_{LK} = 0.75$ into a $L_H^4 K_D$ structure with $D_L = 1.18$, but with a different lattice spacing from the above crystal-crystal transformation. (Fig. 2.10e-f) These tetrahedral geometric transformations provide a simple mechanism to selectively disorder a single monolayer within a crystal structure. . These order-disorder transitions are significant because they involve only the key sublattice. Although the key sublattice transformation is significant, reentrant behavior *Bubeck et al.* (1999) is not observed since the building block transformation implies a connection between two different material systems.

2.4.5 Conclusions

The results shown here suggest that reconfigurable lock-and- key colloidal building blocks have a rich phase space containing structures not seen previously in colloidal crystals. We demonstrate how the combined use of anisotropic and dynamic colloids allow for the design of nontrivial crystal structures such as aperiodic crystals, mixed shaped tiles, and non-compact porous assemblies.

Importantly, we have described possible phases of a recently proposed new class of colloidal molecules *Wang et al.* (2012) with reconfigurability dimensions that can be toggled on demand such as number of locks N_L, bond length d_{LK}, size ratio D_L/D_K, reconfigurability rate, and spatial confinement. These dimensions allow for control over particle coordination, nonadditivity and geometric isomerization, and

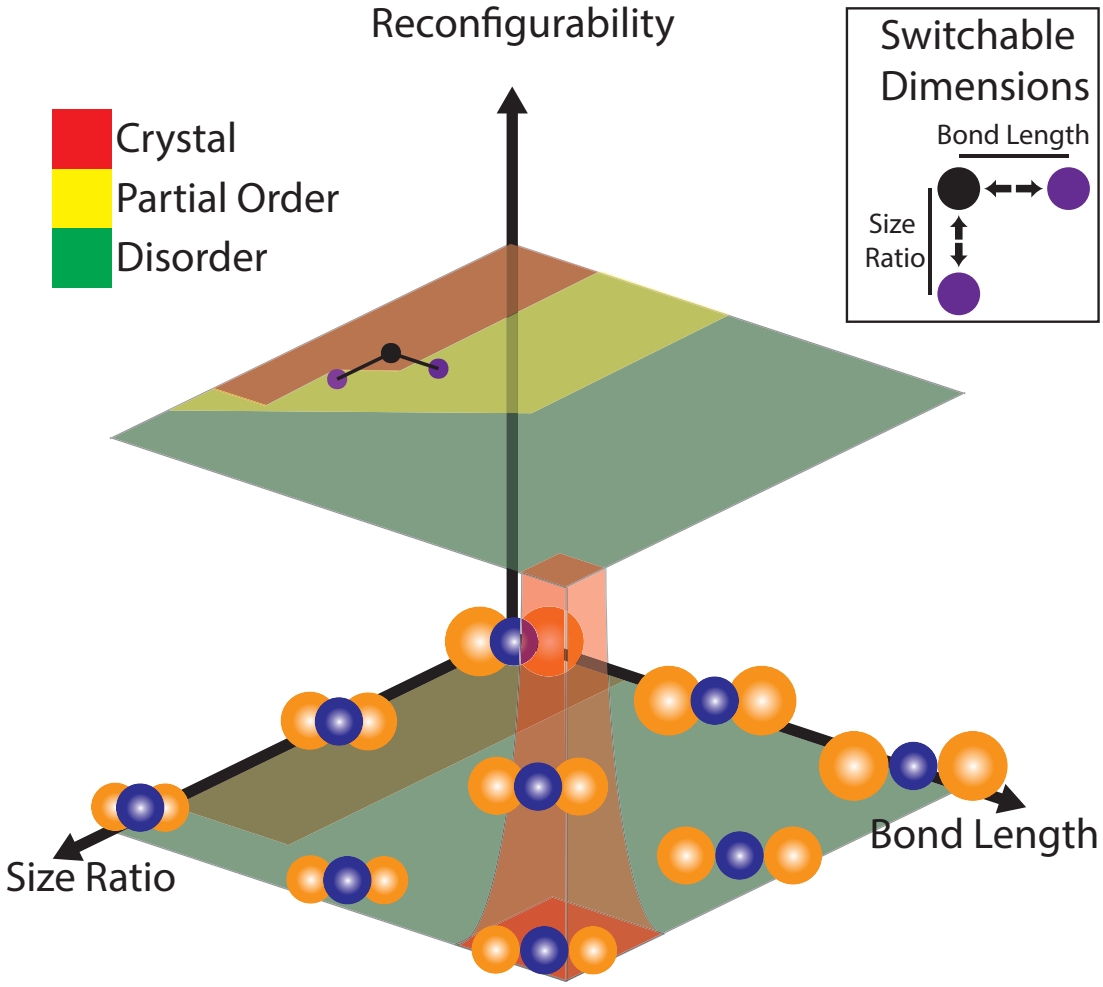

Figure 2.11: The effect of reconfigurability, bond length, and size ratio on molecular colloids is summarized above. Representative building blocks for a range of size ratio and bond length are shown for 2-lock building block. Two different planes of reconfigurability highlight the new crystalline structures that emerge, and the effect of reconfigurability on stability regions. Crystalline structures (red), plastic crystals (yellow), and disorder (green) form. State points (purple and black dots) are chosen from the high reconfigurability layer to highlight how switchable multifunctional nanoparticles are designed. An inset highlights the switchable dimensions of the extended reconfigurability diagram.

lead to many exciting, unexpected, and potentially functional, structures. Additionally, design paths for switchable materials, due to the proximity of photonically active geometric state points such as $L^2_{ATS}K_D$ (Fig. 2.3, 2.4,2.5,2.6), highlight how reconfigurability dimensions such as bond distance or size ratio could be toggled to create colloidal materials with switchable properties. (Fig. 2.11) Responsive thin films such as these could have desirable photonic properties. *Hatton et al.* (2010); *Zhang et al.* (2011b) By altering the confinement of the assemblies, reconfigurable binary nanoparticle superlattices can be assembled. Reconfigurability dimensions provide a framework for the emergence of new crystalline structures, and the rational design of multifunctional colloidal materials.

Finally, even with the systematic study of several reconfigurability dimensions presented here, there remain large tracts of phase space to explore. Switching between two-dimensional and three-dimensional building blocks looks to be a promising direction for the design of omnidirectional optically active materials. . Explorations in 3D assembly could release packing frustrations observed in 2D. The incorporation of higher degrees of shape anisotropy into the lock-and-key building blocks has the potential to generate novel materials and unlock new reconfigurability dimensions. Next-generation building blocks could include the use of ellipsoidal keys with matching locks, patchy keys that allow for tighter control of the coordination of the building blocks, and even the incorporation of colloidal locks that have shape-shifting properties.

CHAPTER III

Self-assembly of Archimedean Tilings with entropically Patchy Polygons

3.1 Abstract

Considerable progress in the synthesis of anisotropic patchy nanoplates (nanoplatelets) promises a rich variety of highly-ordered two-dimensional superlattices. Recent experiments of superlattices assembled from nanoplates confirm the accessibility of exotic phases and motivate the need for a better understanding of the underlying self-assembly mechanisms. Here, we present experimentally accessible, rational design rules for the self-assembly of the Archimedean tilings from polygonal nanoplates. The Archimedean tilings represent a model set of target patterns that (i) contain both simple and complex patterns; (ii) are comprised of simple regular shapes; and (iii) contain patterns with potentially interesting materials properties. Via Monte Carlo simulations, we propose a set of design rules with general applicability to one- and two-component systems of polygons. These design rules, specified by increasing levels of patchiness, correspond to a reduced set of anisotropy dimensions for robust self-assembly of the Archimedean tilings. We show for which tilings entropic patches alone is sufficient for assembly, and when short-range enthalpic interactions are required. For the latter, we show how patchy these interactions should be for optimal

yield. This study provides a minimal set of guidelines for the design of anisostropic patchy particles that can self-assemble all 11 Archimedean tilings.

3.2 Introduction

Tessellations comprised of regular polygons that completely tile the two-dimensional Euclidean plane have been studied since ancient times due to their mathematics and visually attractive symmetries.*Grünbaum and Shephard* Johannes Kepler identified 11 plane-filling tilings known as the Archimedian tilings (ATs),*Kepler* (1942) which can be divided into two groups, namely regular (Figure 3.1a-c) and semi-regular tilings (Figure 3.1d-k) made from regular polygons. The regular tilings are characterized by the ability to map flags (tuples of mutually incident vertices, edges and tiles) via tiling-related group symmetry actions (flag-transitivity), while the remaining semi-regular tilings are expanded with a more relaxed symmetry in mapping vertex pairs to each other by an acting group symmetry pertaining to the tiling (vertex-transitivity).*Grünbaum and Shephard*

Various materials on multiple length-scales are known to form the ATs, which exhibit striking photonic *Ueda et al.* (2007) and diffusive properties. *Basnarkov and Urumov* (2006) The (4.6.12) and (3^2.4.3.4) ATs possess complete photonic band gaps. *Ueda et al.* (2007) Regular and semi-regular tilings are commonly observed in bulk solids, polymeric assemblies, and nanomaterials. Archimedean crystalline nets such as in Al_20_3 (6^3) and $CuAl_2$ (3^2.4.3.4) describe the coordination polyhedra in various crystals of complex alloys.*O'Keeffe and Hyde* (1980) The more complex semi-regular tilings have been observed in the bulk structure of metallic alloys *McMahon et al.* (2000) and supramolecular interfacial tessellations.*Schlickum et al.* (2008); *Tahara et al.* (2006) Manifestations of regular and semi-regular tilings have been observed in liquid crystal *Chen et al.* (2005) (T-shaped molecules) and polymer systems *Takano et al.* (2005) (ABC star branched polymers), and in systems of patchy nanocrystals.

Talapin et al. (2009) The self-assembly of polystyrene spheres in the presence of a decagonal quasicrystalline substrate has been shown to self-assemble the $(3^3.4^2)$ and (3^6) ATs. *Mikhael et al.* (2008) Patchy triblock Janus colloids self-assemble the (3.6.3.6) AT. *Chen et al.* (2011) Most of those results represent the ATs in a vertex-to-vertex representation where particle centers are placed at the vertices of the polygons in the tiling. The diversity of nanoscopic and microscopic components that assemble ATs motivates a need to understand the minimal design rules needed for the assembly of these tilings, in particular from readily accessible 2D nanoplates.

Anisotropic 2D nanoplates are known to have interesting electronic *Ithurria et al.* (2011), catalytic *Kavan et al.* (2011), and optical *Lu et al.* (2006) properties, and have been shown to successfully form exotic superlattices via a subtle balance between shape-induced entropic patchiness *van Anders et al.* (2013c) and ligand-induced enthalpic patchiness. *Ye et al.* (2013c); *Al-Saidi et al.* (2012) 2D assemblies of nanoplates could be used in thin film electronics.*Ando et al.* (2007) Also, 2D assemblies of pervoskites nanoparticles, such as PbTiO3 nanoplates,*Chao et al.* (2013) have interesting ferroelectric and storage properties.*Kim et al.* (2010) Given their polygonal shape, faceted nanoplates could potentially self-assemble the ATs. Although assemblies of ATs from polygonal nanoplates have been reported in experiments, *Sau and Murphy* (2005); *Lee et al.* (2006); *Park et al.* (2006); *Li et al.* (2010); *Ye et al.* (2010); *Shen et al.* (2012b); *Sun and Xia* (2002); *Chen et al.* (2007b); *Paik et al.* (2011); *Zhang et al.* (2005a) they are restricted to the regular ATs (those comprised of a single type of tile) (Figure 3.2). Because faceted nanoplates can exploit both entropic and enthalpic patchy interactions, they represent a viable approach that could reduce the complexity of the design rules for self-assembly of elusive irregular and porous tilings, when compared to the vertex-to-vertex approach.

Numerical simulations have also predicted the self-assembly of the Archimedian tilings. For spherical particles, simulations of patchy particles*Antlanger et al.* (2011);

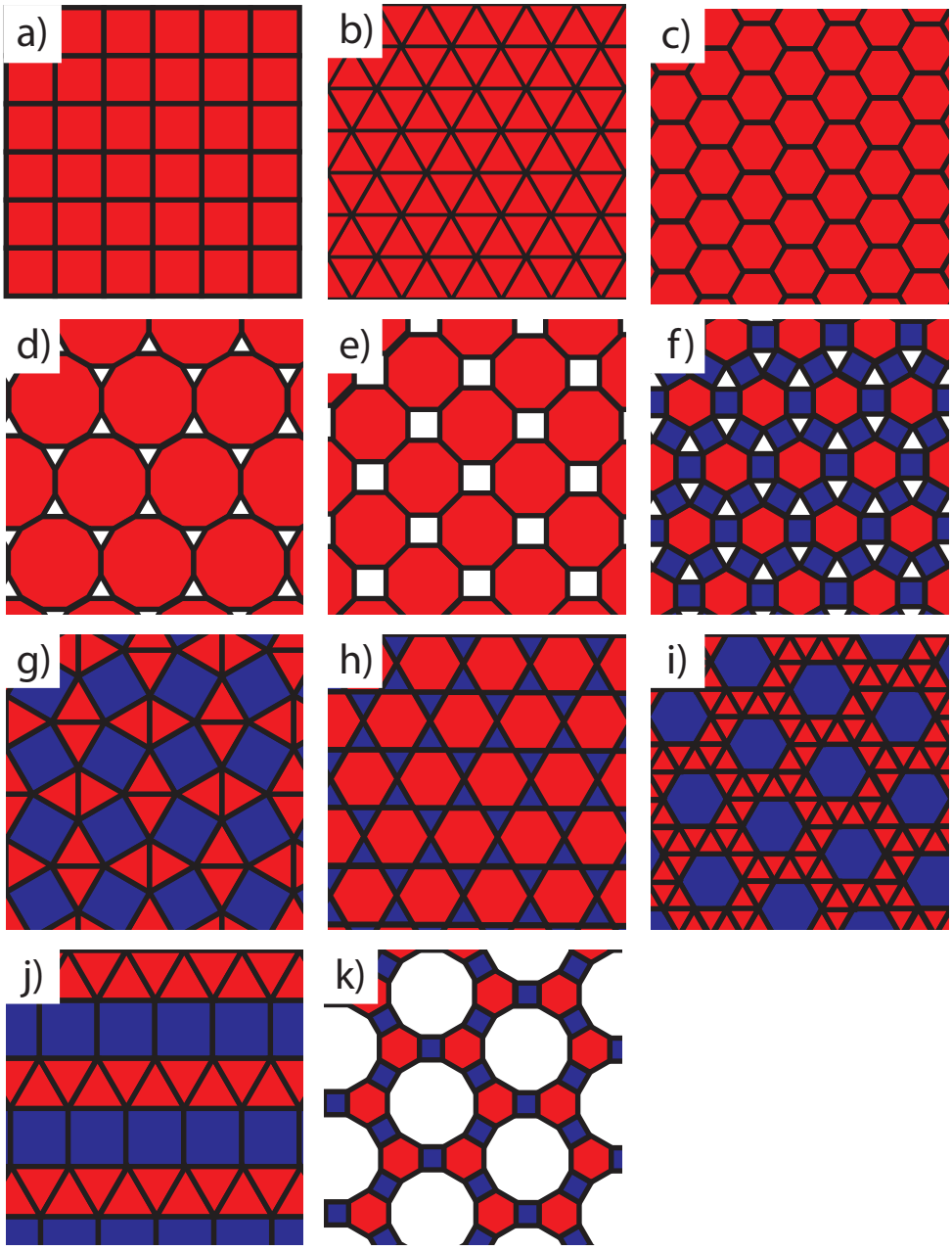

Figure 3.1: The eleven space filling Archimedian tilings. Regular tilings: (a) square (4^4), (b) triangular (3^6), (c) hexagonal (6^3). Semi-regular tilings: (d) truncated hexagonal (3.12^2), (e) truncated square (4.8^2),(f) rhombi-trihexagonal (3.4.6.4), (g) snub square ($3^2.4.3.4$), (h) trihexagonal (or kagome) (3.6.3.6), (i) snub hexagonal tiling ($3^4.6$), (j) elongated triangular ($3^3.4^2$), and(k) truncated trihexagonal (4.6.12) tilings which comprise the entire family of Archimedean tilings.

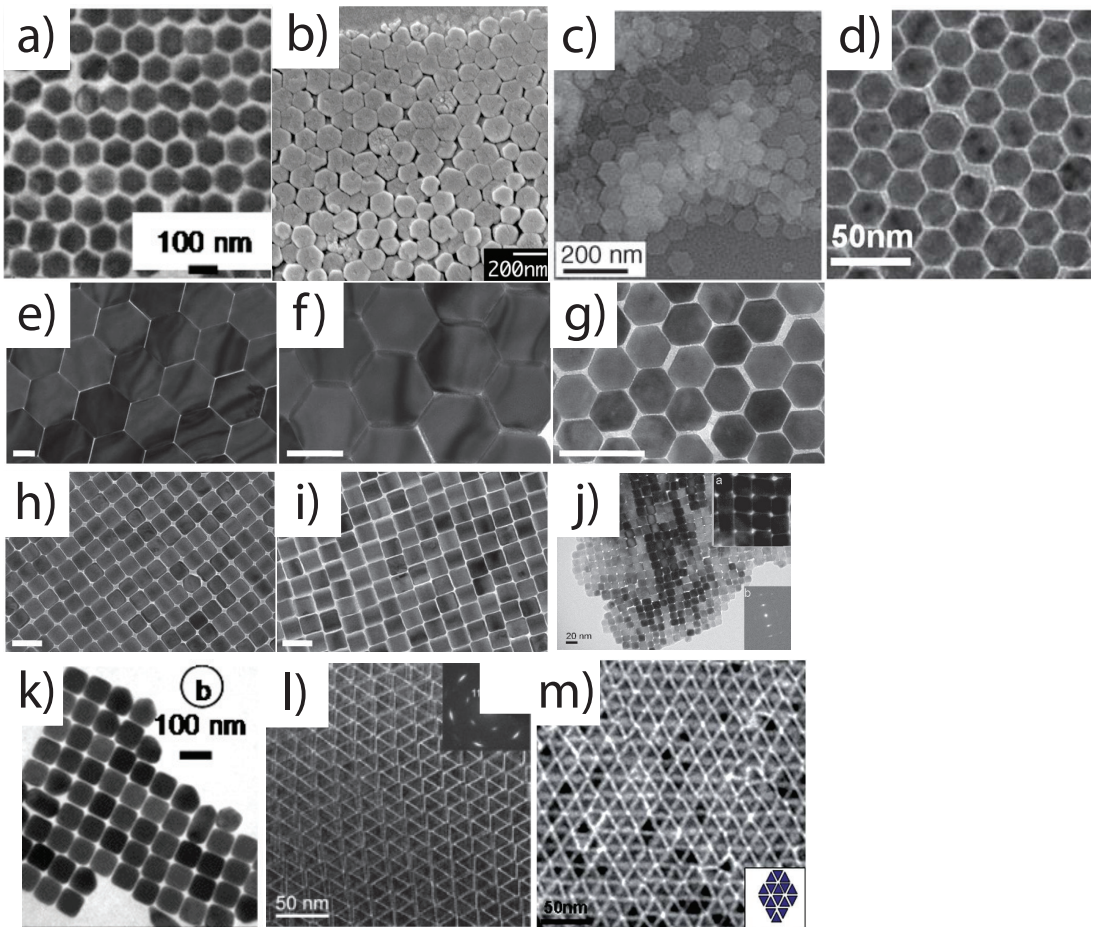

Figure 3.2: Representative snapshots of experimental assemblies of the triangular (3^6), square(4^4), and hexagonal(6^3) ATs. The experimental AT observed are (a) a Au (6^3) AT *Sau and Murphy* (2005), (b) a zeolite ZSM-2 (6^3) AT *Lee et al.* (2006), (c) a In_2S_3 (6^3) AT *Park et al.* (2006), (d) a $Cu_{2-x}Se$ (6^3) AT *Shen et al.* (2012a), (e) a $\beta - NaYF_4$ (6^3) AT *Ye et al.* (2010), (f) a $NaYF_4$: Yb/Er (6^3) AT *Ye et al.* (2010), (g) a $NaYF_4$: Yb/Ce/Ho (6^3) AT *Ye et al.* (2010), (h) a (4^4) $\beta - NaYF_4$ AT *Ye et al.* (2010), (i) a $NaYF_4$: Yb/Er (4^4) AT *Ye et al.* (2010), (j) a TiO_2 (4^4) AT *Chen et al.* (2007b) (k) a Au (4^4) AT55, (l) LaF_3 (3^6) AT *Sau and Murphy* (2005), (m) and a $Cu_{2-x}Se$ (3^6) AT. *Shen et al.* (2012a)

Pawar and Kretzschmar (2010) reported the self-assembly of all ATs except for the (3.6.3.6) AT. Ditethered nanospheres *Iacovella and Glotzer* (2009) formed the (4.8^2) and (6^3) ATs. Lock and key colloids *Sacanna et al.* (2010) and hard polyhedra *Haji-Akbari et al.* (2009); *Damasceno et al.* (2012a) formed the ($3^2.4.3.4$) and (6^3) ATs, respectively. Despite these studies, numerical simulations have neglected the commonly synthesized polygonal nanoplates as a means of AT self-assembly.

A variety of design strategies can be used to improve the self-assembly properties of a nanomaterial. Self-assembly pathway engineering has been used to optimize the assembly properties of patchy particles.*Jankowski and Glotzer* (2012) The inverse optimization of interaction potentials has been shown to improve the assembly properties of soft matter systems *Torquato* (2009). Crystal symmetry can be exploited in the inverse engineering algorithms of target crystal structures. *Cohn and Kumar* (2009) A linear stability analysis using dynamical system theory has been shown to be good predictors of ground state patterns.*VON BRECHT et al.* (2012) Early time correlation and response functions have been shown to be a good predictor of the yield of a crystalline structure in self-assembly.

Here, we report the minimal set of interactions needed to self-assemble experimentally accessible ATs from regular polygons, mimicking nanoplates assembled into crystalline monolayers (Figure 3.2). We show through Monte Carlo simulations the self-assembly of these tilings by exploiting entropic and enthalpic interactions encoded in the shape of the polygons. We arrive at a design strategy for patchy polygon particles that is accessible to current experimental techniques, and present the minimal set of design rules for each AT. We report that four ATs, namely the (6^3), (3^6), (4^4), and (3.12^2) tilings, can be assembled solely with hard interactions, highlighting the role of directional entropic forces *Damasceno et al.* (2012a); *van Anders et al.* (2013a) that arise from the particle shape. We quantify the strength of these entropic patches *van Anders et al.* (2013a) by calculating the potential of mean force

and torque using free energy calculations. *van Anders et al.* (2013a) Symmetric enthalpic patches ((4.8^2)), shape specific patches ($(3^2.4.3.4)$, (3.4.6.4), (3.6.3.6)), and edge specific patches ($(3^3.4^2)$, $(3^4.6)$, (4.6.12)) are needed to self-assemble the remaining crystalline structures. Beyond the ATs, the design rules presented provide general insight into the design of complex crystal structures using anisotropic building blocks.

3.3 Model

Each nanoplate is modeled as a hard convex regular polygon with a finite number of edges N = 3, 4, 6, 8 and 12. In the first model -that of least complexity- no additional interactions are included. Initially, we find those ATs ((3^3), (4^4), (6^3), (3.12^2)) that can be assembled by entropic forces alone. In all cases, shape anisotropy gives rise to entropic patchiness that emerges upon crowding and is density dependent. *van Anders et al.* (2013a)

For the remaining ATs, we introduce a short-range attractive edge-to-edge interaction potential. The interaction potential is divided into parallel, perpendicular and angular components (Figure 3.3b). The parallel component represents the amount of parallel contact between interacting edges. The perpendicular component models the commonly-observed attractive van der Waals force between ligand-capped nanocrystals. *Schapotschnikow et al.* (2008); *de Vries* (2006); *Kaushik and Clancy* (2012) This component is dependent on the distance between centers of edges and is approximated by a parabolic well. The angular component penalizes any misalignment between neighboring nanoplates representing steric forces between ligand shells. A halo drawn around the building block represents the interaction range of the edge-edge pair potential (Figure 2.3a). Different colors represent different interaction strengths between edges. These enthalpic patches act as reversible, directional, sticky bonds that compete or combine with entropic patches. The justification of such a short-range potential in a nanoplate system is based on the presence of adsorbed ligands

(e.g. oleic acid molecules).*Ye et al.* (2013c,a)

The complexity of the edge-to-edge interactions is determined by the targeted AT. We found that we need three enthalpic models of increasing complexity for the assembly of the remaining ATs: symmetric, shape-specific and edge-specific. The first enthalpic model treats the pairwise interaction between polygons as patches of equal strength distributed over all edges. The second enthalpic model (shape-specific), which is a modification of the previous model, tunes the interaction strength between patches of dissimilar polygons for those ATs comprised of binary tile mixtures. The third enthalpic model (edge-specific) further increases the interaction complexity and determines the interaction strength based on the type of edges even for similarly shaped particles. To quantify the interaction asymmetry between different edges, we introduce the parameter σ. The σ values reported are the minimum asymmetry needed to assemble the target ATs. For each AT tiling, we find a favorable thermodynamic state point for self-assembly of the building block.

3.4 Methods

Nanoplates are represented as hard polygons, and simulated using an NPT MC algorithm. The pressure was slowly increased over time. Overlap checks were performed using the GJK algorithm.*Gilbert et al.* (1988) NVT simulations were performed for simulation runs with attractive short-range forces. The number of particles was varied between 900 to 2000 to ascertain the absence of finite size effects. We equilibrated each simulation for 10^7 time steps and also gathered statistics for 10^7 timesteps using established Monte Carlo methods.*Ye et al.* (2013c)

We computed the tendency for particles to align entropically via the entropic potential of mean force and torque.*van Anders et al.* (2013a) We considered a pair of polygons in a sea of other polygons, and denote nearby relative positions and orientations of the pair by $\Delta\xi_1$ and $\Delta\xi_2$. The free energy difference for the sea particles

between these two states is given by the logarithm of the ratio of the number of microstates available to the sea when the pair is in the configuration $\Delta\xi_1$ to the number of microstates when it is in the configuration $\Delta\xi_2$, which we denote by $\Omega(\Delta\xi_1)$ and $\Omega(_2)$ respectively. To evaluate this ratio we note that some microstates in $\Omega(\Delta\xi_1)$ will also be in $\Omega(\Delta\xi_2)$. The number of such states will be proportional to the probability that a randomly selected state in $\Omega(\Delta\xi_1)$ is also in $\Omega(\Delta\xi_2)$. To determine this probability we fix a pair of tiles at $\Delta\xi_1$, and compute the probability that a trial move to $\Delta\xi_2$ is accepted $p(\Delta\xi_1 \to \Delta\xi_2)$. We also determine the probability $p(\Delta\xi_2 \to \Delta\xi_1)$ of the reverse move from $\Delta\xi_2$ to $\Delta\xi_1$. In addition we must also take into account the difference in infinitesimal volumes available to the pair at a given relative position and orientation. The PMFT difference is then given by

$$\exp^{-\beta(F_{12}(\Delta\xi_1)-F_{12}(\Delta\xi_2))} = \frac{J(\Delta\xi_1)p(\Delta\xi_1 \to \Delta\xi_2)}{J(\Delta\xi_2)p(\Delta\xi_2 \to \Delta\xi_1)} \tag{3.1}$$

3.5 Results

We present our findings in four categories based on the four types of interaction sets needed to assemble the Archimedean tilings: (i) entropic, (ii) symmetric, (iii) shape-specific and (iv) edge-specific enthalpic interactions. All ATs can be self-assembled with these four interaction approaches. The results are summarized in Figures 3.4 and 3.10.

3.5.1 Entropic Interactions

Directional entropic forces arising from shape entropy, or a drive to local dense packing, are an entropic strategy to self-assemble the Archimedean tilings. *van Anders et al.* (2013a) In our studies, by changing the number of vertices of the building block,

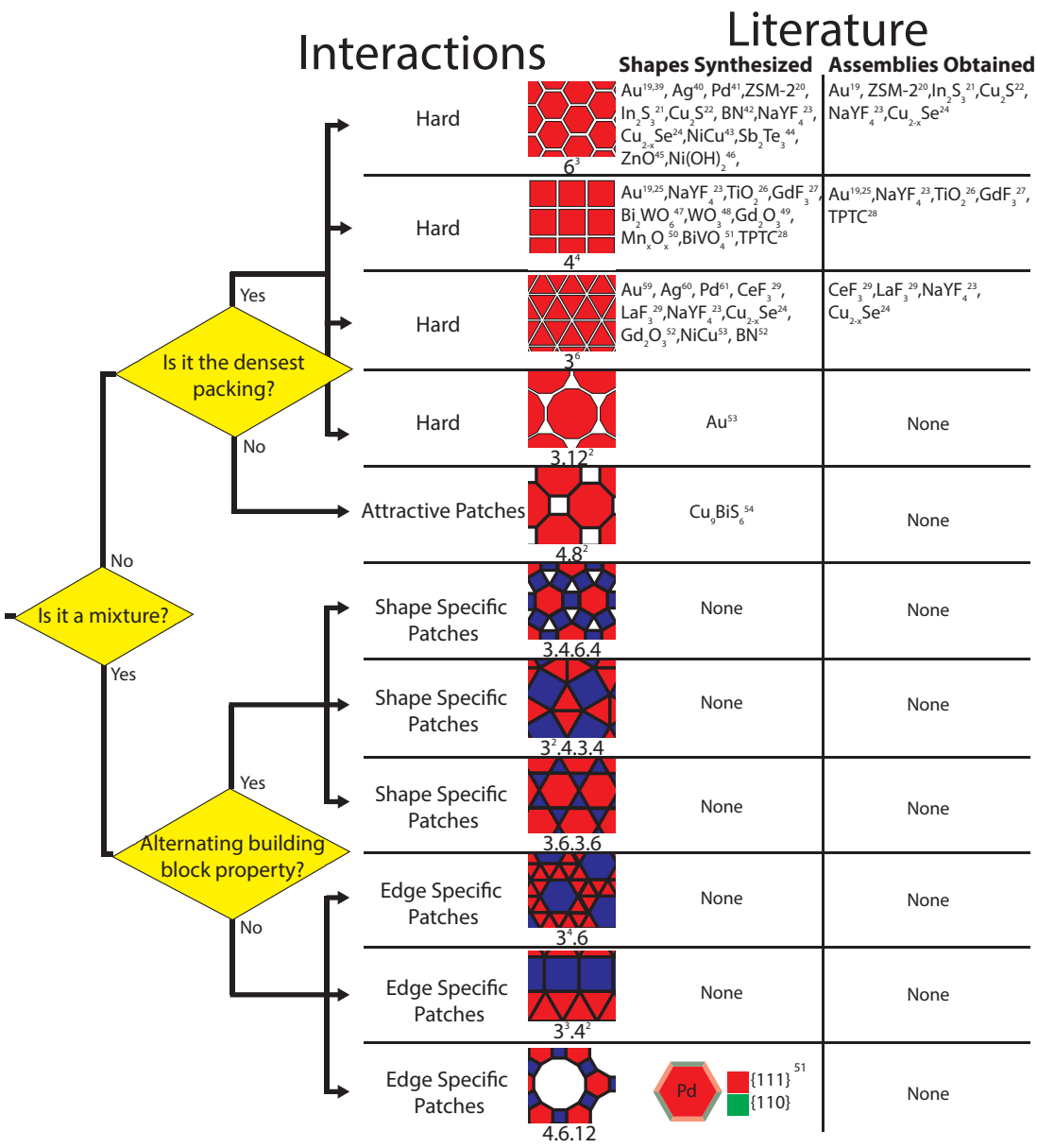

Figure 3.3: Flow diagram representing the design process for the ATs. The paths show how to self-assemble the ATs. Hard interactions are for assemblies that coincide with their densest packings in single component systems. Shape specific patches are for mixtures with lines of alternating building blocks. Mixtures with complex bond networks need edge specific patches. The two rightmost columns show the state-of-the-art in particle synthesis and self-assembly for each corresponding AT.

regular polygons are shown to self-assemble four of the ATs. Regular triangles and squares form the (3^6) and (4^4) ATs (Fig. 3.4a,b).

Regular triangles and squares form the (3^6) and (4^4) ATs, respectively (Figure 3.5a,b). Insets show the regular polygon building block and a close-up of the assembly. The accompanying diffraction patterns show sharp peaks in hexagonal and square reciprocal lattices for triangles and squares, respectively, as a manifestation of long-range order. The small number of defects highlights the robustness of the assembly of both regular triangular and square tilings. However, there exists a collection of crystalline structures that differ from the triangle and square ATs solely by a shift vector along the lattice axes. Although at infinite pressure all of these tilings belong to a thermodynamically stable degenerate set with equal probability for self-assembly, we observe that at finite pressures the (3^6) and (4^4) ATs are the equilibrium configurations. Previous work has also shown that the equilibrium structures of hard triangles and squares at high packing fractions are the (3^6) and (4^4) ATs, respectively.*Wojciechowski and Frenkel* (2004); *Zhao et al.* (2011, 2012) Hard hexagons readily form the (6^3) AT (Figure 3.5c) at finite pressures. This is the unique infinite pressure (maximum density) crystal structure for the regular hexagon due to shape constraints.

All of the ATs are, by definition, space filling. However, by treating some tile types as pores, it is possible to assemble some multi-tile ATs with a single nanoplate shape. An example of this is the (3.12^2) AT, which is comprised of dodecagons and triangles. We find that regular dodecagons easily self assemble into the truncated hexagonal Archimedean tiling at finite pressures without explicit triangle tiles; that is, treating the triangles as pores in the tiling (Figure 3.5d). Notably, this assembly is also the infinite pressure crystal for hard dodecagons.*Duparcmeur* (1995)

To summarize the results thus far, for each of the four (regular) ATs just discussed, entropy alone is sufficient to obtain the tiling via thermodynamic self-assembly. This

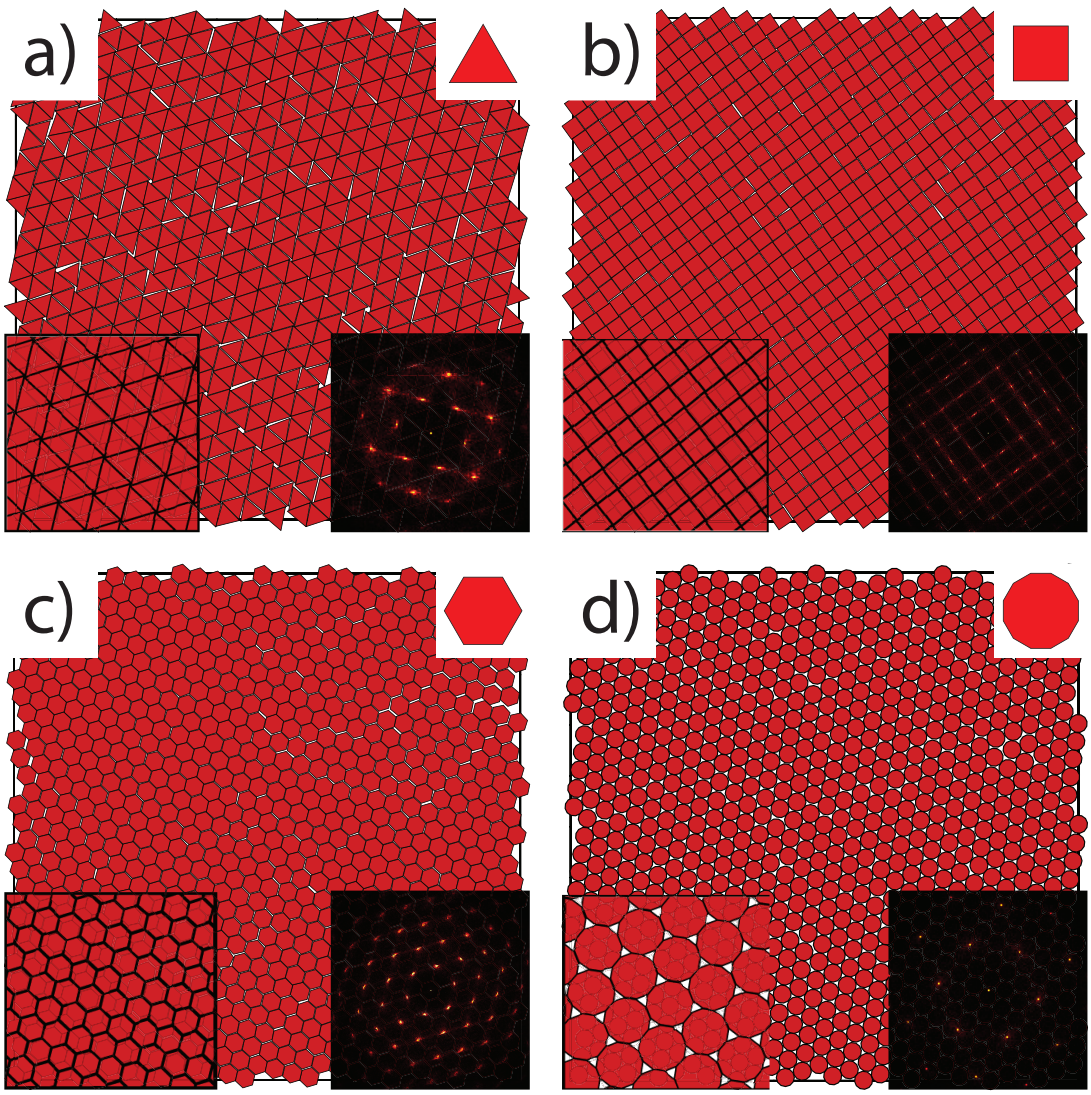

Figure 3.4: We show representative snapshots of simulations for the (3^6), (4^4),(6^3),(3.12^2). ATs self-assembled with excluded volume interactions only. Each assembled Archimedean tiling is accompanied by an inset showing the polygonal particle, a diffraction pattern of the snapshots, and a compressed close-up. We show that a triangles self-assemble the (3^6) tiling at a packing fraction equal to 0.90 (a), a squares self-assemble the (4^4) tiling at a packing fraction 0.94 (b), hexagons self-assemble the (6^3) tiling at a packing fraction 0.93 (c) and dodecagons self-assemble the (3.12^2) tiling at packing fraction 0.85 (d).

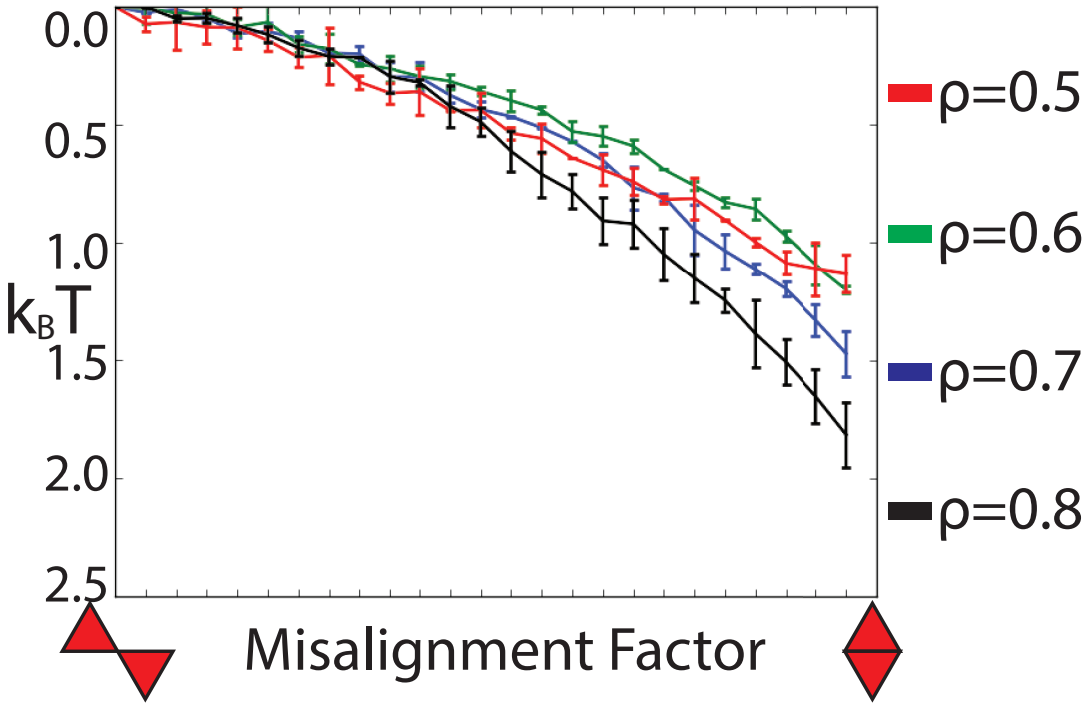

Figure 3.5: Effective free energy difference between different configurations of hard triangles as a function of density is shown above. We show the free energy difference as a function of the misalignment factor f. The blue line shows the free energy gain by aligning the edges of the triangles. We show the free energy increases for densities equal to 0.5(a), 0.6(b), 0.7(c), and 0.8(d). The free energy gain is $1.2k_BT$, $1.2k_BT$,$1.5k_BT$, and $1.8k_BT$ at packing fraction values of 0.5 , 0.6 , 0.7 and 0.8, respectively.